ESPOO 2003 VTT PUBLICATIONS 493

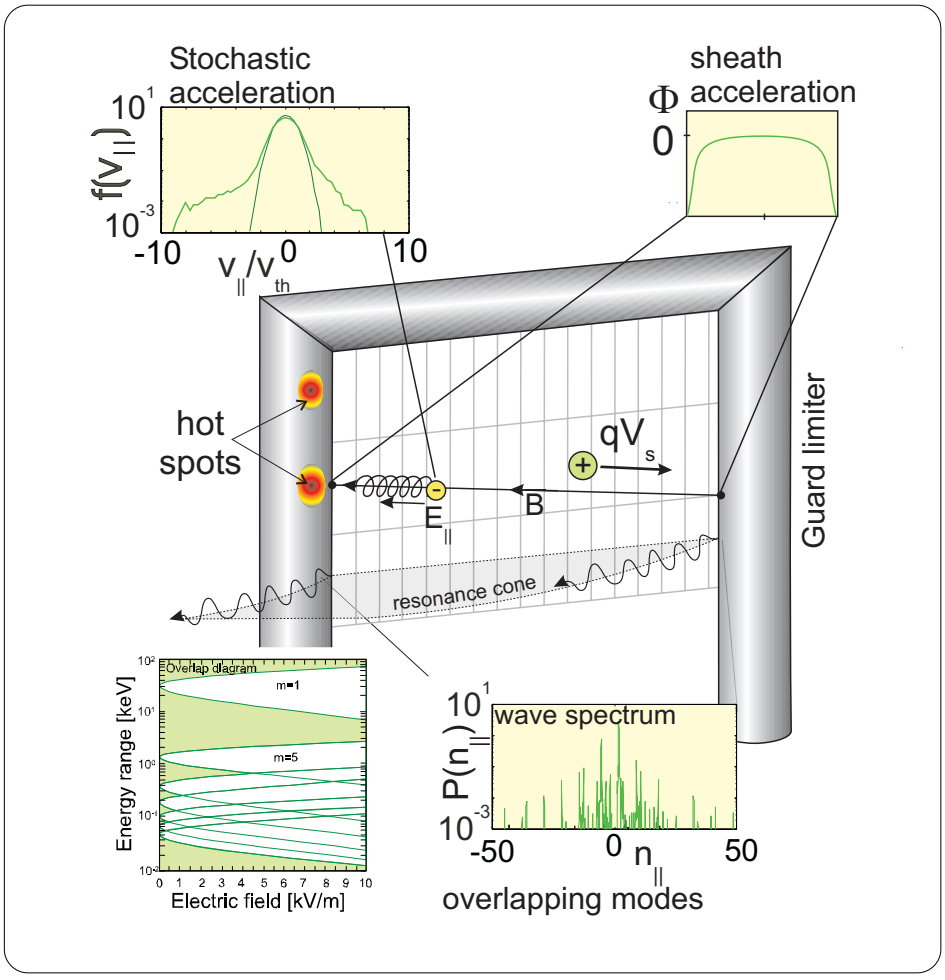

Karin Rantamäki

Particle-in-Cell Simulations of the Near-Field of a Lower Hybrid Grill

VTT PUBLICATIONS 493

Particle-in-Cell Simulations of the Near-Field of a Lower Hybrid Grill

Karin Rantamäki

VTT Processes

Dissertation for the degree of Doctor of Science in Technology
to be presented with due permission for public examination and debate
in Auditorium F1 at Helsinki University of Technology (Espoo, Finland)
on the 23rd of May, 2003, at 12 o'clock noon.

ISBN 951–38–6040–X (soft back ed.)
ISSN 1235–0621 (soft back ed.)

ISBN 951–38–6041–8 (URL: http://www.inf.vtt.fi/pdf/)
ISSN 1455–0849 (URL: http://www.inf.vtt.fi/pdf/)

JULKAISIJA – UTGIVARE – PUBLISHER

VTT, Vuorimiehentie 5, PL 2000, 02044 VTT
puh. vaihde (09) 4561, faksi (09) 456 4374

VTT, Bergsmansvägen 5, PB 2000, 02044 VTT
tel. växel (09) 4561, fax (09) 456 4374

VTT Technical Research Centre of Finland, Vuorimiehentie 5, P.O.Box 2000, FIN–02044 VTT, Finland
phone internat. + 358 9 4561, fax + 358 9 456 4374

VTT Prosessit, Otakaari 3 A, PL 1608, 02044 VTT
puh. vaihde (09) 4561, faksi (09) 456 6390

VTT Processer, Otsvängen 3 A, PB 1608, 02044 VTT
tel. växel (09) 4561, fax (09) 456 6390

VTT Processes, Otakaari 3 A, P.O.Box 1608, FIN–02044 VTT, Finland
phone internat. + 358 9 4561, fax + 358 9 456 6390

Technical editing Maini Manninen

Otamedia Oy, Espoo 2003

Rantamäki, Karin. Particle-in-Cell Simulations of the Near-Field of a Lower Hybrid Grill. Espoo 2003. VTT Publications 493. 74 p. + app. 61 p.

Keywords plasma heating, microwaves, lower hybrid grill, lower hybrid waves, particle-in-cell simulation, parasitic absorption, wave coupling, thermonuclear devices, Tore Supra, tokmak, JET, current drive, nuclear fusion

Abstract

Lower hybrid (LH) waves in the frequency range 1 to 10 GHz are used to heat and to drive current in a tokamak. A crucial issue for the future devices is the coupling of the wave power from the launching structure, the grill, to the plasma. A related problem is the formation of hot spots on the grill limiters and other components that are magnetically connected to the grill region. A probable explanation for these asymmetric heat loads is the parasitic absorption of the LH power. In parasitic absorption, the short-wavelength modes are absorbed by electrons within a very short distance in front of the grill. The cold edge electrons ($T_e \sim 25$ eV) may reach energies up to 2 keV through stochastic acceleration in the electric field in front of the lower hybrid grill.

The particle-in-cell (PIC) technique is one of the most popular methods of kinetic simulations of plasmas. In PIC codes, a spatial grid is used to describe the field quantities, while the particles move in the continuous space. The field and particle motion are solved self-consistently. The advantage of the PIC codes is that they take into account the kinetic effects and the non-linearities of the problem. They also give the deposition profiles unlike pure test particle simulations.

In this thesis, the use of PIC codes has been extended to a whole new branch of applications, the near-field of the LH grill. During the work, the grill model used in the electrostatic PIC code has been developed. The parasitic absorption and the generation of fast electrons in front of the waveguide mouth have been explored. The absorption and the heat load on the grill limiter increases with the edge density, the edge temperature and the launched power density. A weak indication of a power threshold was observed. The simulation results can explain experimental observations in Tore Supra. According to the simulations, the heat loads are not a problem in the next generation launchers used in ITER.

Preface

The work presented in this thesis has been carried out at VTT and at the Laboratory of Advanced Energy Systems, at the Helsinki University of Technology. The work was part of the FFusion 2 Technology Programme under the Association Euratom–Tekes.

I wish to express my gratitude to Dr. Seppo Karttunen, Head of the Research Unit of the Association Euratom–Tekes, and Professor Rainer Salomaa for giving me the opportunity to work within the research field of fusion and plasma physics. I also thank them for suggestions for improving the manuscript. I am indebted to my instructor Dr. Timo Pättikangas for his invaluable guidance and support during this thesis. He was always there patiently answering my questions and explaining the physics. I also wish to thank him for the critical and careful reading of the manuscript.

During the work I had the opportunity to work at Tore Supra for a while. The time I spent there was very fruitful, I learned a lot there and had a very good time both at work and outside. I wish to thank everyone at CEA Cadarache who made this stay there possible and pleasant, and the European Commission that supported the visits under the Staff Mobility Agreement. I am grateful to Dr. Xavier Litaudon and Dr. Didier Moreau for suggesting the interesting subject of this thesis, namely the hot spot problem. I thank them also for their good guidance during my stay in Cadarache. In addition, I wish to thank Dr. Marc Goniche for his enthusiasm and encouragement, as well as Dr. Philippe Bibet for providing me with the SWAN results and for his interest in the work.

I am grateful to Minna Tuomainen and Seppo Kelppe with his family, for making my stay in France so pleasant. In Cadarache, I also became acquainted with Dr. Vladimir Fuchs from IPP Prague. We had many nice discussions about PIC simulations and plasma physics, which I will warmly remember, as well as the nice dinners on the solar terrace of our hotel in Aix-en-Provence with him and Susie.

I had the possibility to spend some time also at the University of Berkeley with the Plasma Theory and Simulation Group. I wish to thank Professors C. K. Birdsall and John Verboncoeur for making this visit possible. All my friends at the I-House, Berkeley, should be thanked for making my stay there such a nice period. The visit was partly supported by the USA/Japan collaboration programme of VTT.

I would like to acknowledge the Plasma Theory and Simulation Group (Professor C. K. Birdsall, University of California, Berkeley) for providing me with their 2d3v PIC-MCC codes XPDP2 and XOOPIC. Professor Siegbert Kuhn is thanked for organising in Innsbruck, Austria both the PDW2 Workshop in 1995 and the Edge Plasma Theory and Simulation Workshops in 1998. Without those Workshops this work would probably never have been realised. In particular, I wish to thank Dr. David Cooperberg and Dr. Venkatesh P. Gopinath for helping me achieve initial runs with XPDP2 as well as John Verboncoeur and Peter Mardahl for the runs with XOOPIC.

The staff at VTT and the Laboratory of Advanced Energy Systems should be thanked for the pleasant working atmosphere especially in the Plasma Physics Group. Special thanks belong to Dr. Taina Kurki-Suonio for the "madame-coffees" and her suggestions in improving this manuscript. Many thanks also to Dr. Tuomas Tala for the nice discussions on orienteering and training.

The Otaniemi Chapel Choir and my friends are warmly thanked for providing me with other activities outside science. Singing in the choir has been very nice and relaxing. Thank you all who have been singing in the choir during the years. Special thanks also to Heli and Antti for the physical activities.

Financial support by Tekes, VTT and the European Commission are gratefully acknowledged. The Centre for Scientific Computing in Espoo, Finland is thanked for their allocation of computer time.

Special thanks belong to Reko, my husband, for his patience and understanding during this work. My parents Käthe and Eero Sarparanta, are thanked for the support and interest in my studies and work.

Espoo, 9th April 2003

Karin Rantamäki

List of Publications

This thesis consists of an introduction and a review of the main results reported in the following publications:

I. K. M. Rantamäki, T. J. H. Pättikangas, S. J. Karttunen, X. Litaudon and D. Moreau, "Generation of hot spots by fast electrons in lower hybrid grills", *Physics of Plasmas* **5** (1998) pp. 2553–2559.

II. K. M. Rantamäki, T. J. H. Pättikangas, S. J. Karttunen, X. Litaudon, D. Moreau, P. Bibet and A. Ekedahl, "Particle-in-cell simulation of parasitic absorption of lower hybrid power in edge plasmas of tokamaks", *Plasma Physics and Controlled Fusion* **41** (1999) pp. 1125-1133.

III. K. M. Rantamäki, T. J. H. Pättikangas, S. J. Karttunen, P. Bibet, X. Litaudon and D. Moreau, "Estimation of heat loads on the wall structures in parasitic absorption of lower hybrid power", *Nuclear Fusion* **40** (2000) pp. 1477–1490.

IV. K. M. Rantamäki, Ph. Bibet, S. J. Karttunen, T. J. H. Pättikangas and X. Litaudon, "Particle-in-Cell Simulations of the New Tore Supra LH Grill", in J. W. Connor, O. Sauter and E. Sindoni (Eds.) *International School of Plasma Physics "Piero Caldirola", Theory of Fusion Plasmas*, (Societa Italiana di Fisica, Bologna, Italy, 2000) pp. 463–468.

V. K. M. Rantamäki, T. J. H. Pättikangas, S. J. Karttunen, K. M. Alm-Lytz, J. P. Verboncoeur and P. Mardahl, "Electromagnetic Particle-in-Cell Simulations of a Lower Hybrid Grill", *Plasma Physics and Controlled Fusion* **44** (2002) pp. 1349–1362.

Publication I introduces the self-consistent particle-in-cell simulations as a tool for studying the behaviour of the plasma in front of the grill mouth. In this first work, a very simple model for the grill is used. The numerical diagnostics to obtain the coupled and absorbed powers are developed.

A more sophisticated model for the grill is used in Publication II. Parasitic absorption of the short wavelength modes of LH power is calculated for both JET and Tore Supra. For Tore Supra the density dependence of parasitic absorption is studied with four different edge densities.

The power and temperature dependence of parasitic absorption is analysed in Publication III. A method for estimating the heat load on the grill limiters is developed and applied to the Tore Supra LH grill.

In Publication IV, the methods developed in the previous papers are used for calculating the parasitic absorption and the heat loads for the new grill of Tore Supra.

Publication V deals with an electromagnetic PIC code. For the first time, a whole grill with 32 waveguides is modelled with particle-in-cell simulations. The coupling of the wave from waveguides to plasma is analysed and the reflection coefficients in the individual waveguides are determined.

The author has actively participated in all the work presented in the above publications. She has performed all the simulations and analysis of the work. She had the responsibility of developing the electrostatic particle-in-cell code to suit the simulations of parasitic absorption. She was the principal author of all the above papers. Other publications related to this thesis with a contribution from the author are [33–35, 37, 39, 77, 79–81, 84–88, 90].

Contents

Chapter 1

Introduction

World Energy Council predicts that the world population doubles in the next 50 years [1]. The two major challenges for the future of the mankind are the availability of clean water and the adequacy of energy. During this century the primary energy use is doubling even according to the most conservative scenario [1]. With the pessimistic scenario, the energy consumption in 2100 will be at a level of almost 5 times that of 1990.

So far, the energy production has been based on natural resources that have accumulated to the ground during millions of years. Most of these are fossil fuels, the main resource being coal. However, these are running towards an end. Moreover, they are considered to enhance the greenhouse effect and causing global warming.

In order to get a sustainable solution to the energy problem, all the possible knowledge is needed as well as a variety of benign energy production methods. No single power production method can meet the energy need by itself. Renewable energy should be used where it is feasible. However, it is not suitable for supplying the base load where nuclear energy could be used instead. The disadvantage of fission energy is its public acceptability. A long term problem is the adequacy of fuel. Together with fission power and the renewable energy sources, thermonuclear fusion can provide a sustainable solution for the power production. The main advantage of fusion is that it has unlimited fuel sources – fifty coffee cups or a bucket full of seawater correspond to 2 tons of coal. An equally important benefit is that it is inherently safe. There is practically no possibility for run-away accidents. The loss of coolant does not lead to a melt-down accident. Drawbacks of fusion are its technical complexity and high costs.

In fusion, two light nuclei fuse together forming a heavier nucleus and releasing energy. This is the energy source of the sun and other stars. To harness this

energy on earth is a demanding task. In terms of energy production in fusion devices, the most important reactions are

$$^2\mathrm{D} + {}^3\mathrm{T} \longrightarrow {}^4\mathrm{He} + {}^1\mathrm{n} + 17.6\ \mathrm{MeV} \tag{1.1a}$$

$$^2\mathrm{D} + {}^2\mathrm{D} \longrightarrow {}^3\mathrm{T} + {}^1\mathrm{p} + 4.03\ \mathrm{MeV} \quad (50\%) \tag{1.1b}$$

$$^2\mathrm{D} + {}^2\mathrm{D} \longrightarrow {}^3\mathrm{He} + {}^1\mathrm{n} + 3.27\ \mathrm{MeV} \quad (50\%) \tag{1.1c}$$

$$^2\mathrm{D} + {}^3\mathrm{He} \longrightarrow {}^4\mathrm{He} + {}^1\mathrm{p} + 18.3\ \mathrm{MeV}, \tag{1.1d}$$

where ^{2}D and ^{3}T are the heavier hydrogen isotopes deuterium and tritium, respectively, n is a neutron, p is a proton, and ^{3}He and ^{4}He are helium isotopes. The energy is released as kinetic energy and it is distributed inverse-proportionally to the masses of the reaction products. The neutrons are beneficial for the energy extraction as they carry most of the energy out of the plasma. On the other hand, the neutron causes activation of the inner structures, which can, however, be reduced with properly choosing the reactor materials.

To get the nuclei close enough, a high temperature is needed so that the Coulomb barrier can be overcome. For the easiest reaction, the D – T reaction, a temperature of about 10 keV, i.e. 100 million degrees is needed in a fusion device. This is about ten times the temperature inside the sun. In addition to the temperature, sufficient density is also needed as well as long enough confinement of the particles and energy to overcome the radiation and diffusion losses from the plasma. The requirement for these three quantities can be written in the form of the so-called triple product [2]

$$n\,T\tau_E > 3 \times 10^{21}\ \mathrm{m}^{-3}\,\mathrm{keV\,s}. \tag{1.2}$$

This is the lower limit for ignition, where the fusion burn becomes self-sustaining. Here, n is the density, T is the temperature and τ_E is the energy confinement time.

At the high temperatures required for fusion, the fuel is in plasma state, a fully ionised quasineutral gas. The high temperature also gives rise to various difficulties and causes the complexity of controlled fusion. The problem is how to confine and insulate the hot plasma. One solution is to use a so-called 'magnetic bottle', where the plasma is confined by magnetic fields. At the moment, the most promising device for a fusion reactor is the tokamak, which was developed in the former Soviet Union in the fifties [2, 3].

The tokamak is based on magnetic confinement, where the particles are bound to the magnetic field lines. Figure 1.1 shows a schematic picture of a tokamak. The device is essentially a solenoid, which has been bent to a torus, thus eliminating the end losses of linear devices. The main component of the magnetic field is the toroidal one. The bending of the field lines introduces drifts like the $\nabla \boldsymbol{B}$ and $\boldsymbol{E} \times \boldsymbol{B}$ drifts that tend to destroy the confinement due to particle flow out of the plasma. In order to balance these outward drifts, the field lines have to be twisted to form a helical field. In tokamaks, this is done by inducing a toroidal current that creates the poloidal field component.

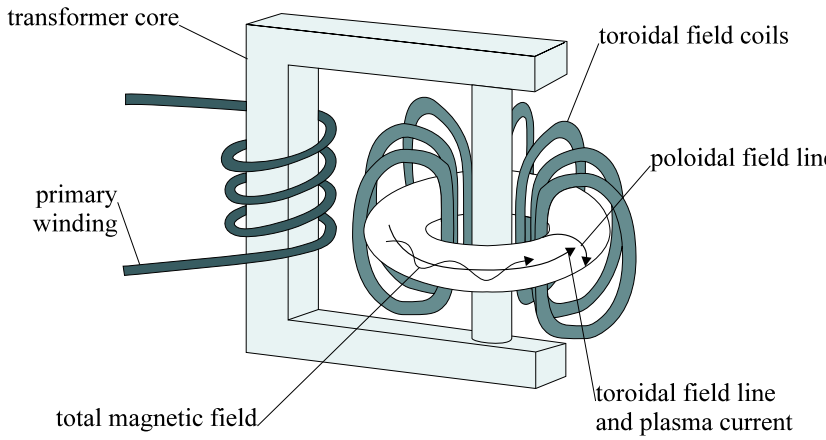

Figure 1.1: The tokamak concept.

As the plasma has a high conductivity, it can be considered as the secondary circuit of a transformer, where the primary winding is an external one, see Figure 1.1. In order to have continuous operation, or at least sufficiently long pulses, non-inductive current drive is needed because otherwise a tokamak can only operate as a pulsed device. The basic idea of current drive is to introduce some kind of asymmetry with respect to the toroidal direction. There are two main methods for doing this. One is the neutral beam injection (NBI) using high-energy neutral particles that penetrate the magnetic field and transfer their momentum to the plasma. The other method, which is investigated in this work, uses electromagnetic waves. The waves are launched from the edge of the plasma and their energy is transferred to the plasma particles through a resonant interaction.

One of the most promising concepts to drive current is the use of lower hybrid (LH) waves at a frequency of a few GHz. The frequency is low enough for high power generators to exist. These generators are called klystrons. On the other hand, it is high enough for the waves to travel through waveguides to the plasma edge, where they are launched. At Tore Supra [4], an LH pulse of 3 min 35 s was recently realised [5]. A total of 600 MJ of energy was injected. The LH power in this pulse was around 3 MW for 215 s.

The LH waves deposit their energy through a resonant interaction to electrons having a somewhat lower velocity along the magnetic field than the corresponding phase velocity of the wave. A change in the parallel velocity of $\Delta v_\parallel$ leads to an increment in the current density, $\Delta j = n_\mathrm{e} q_\mathrm{e} \Delta v_\parallel$, and a change in energy density of $\Delta E = n_\mathrm{e} m_\mathrm{e} v_\parallel \Delta v_\parallel$, where m_e, q_e and n_e are the electron mass, charge and density, respectively [6, 7]. Here, parallel refers to the direction of the magnetic field. The current lasts for a time $1/\nu_\mathrm{c}$, where ν_c is the collision frequency. The power density required to refresh the current is therefore

$$\mathcal{P}_\mathrm{RF} = \frac{\Delta E}{\Delta t} = n_\mathrm{e} m_\mathrm{e} v_\parallel \Delta v_\parallel \nu_\mathrm{c} \tag{1.3}$$

and the steady-state current drive efficiency

$$\eta = \frac{J}{P} = \frac{\Delta j A_{\mathrm{pol}}}{\mathcal{P}_{\mathrm{RF}} V} = \frac{q_{\mathrm{e}}}{2\pi R m_{\mathrm{e}} v_{\parallel} \nu_{\mathrm{c}}}, \tag{1.4}$$

where $V = 2\pi R A_{\mathrm{pol}}$ is the plasma volume, A_{pol} is the poloidal surface and R is the major radius of the tokamak.

From this equation it can clearly be seen that the current drive efficiency is maximised by minimising the quantity $v_{\parallel}\nu_{\mathrm{c}}$. There are two limits to this [6]. The first one is the low velocity limit, where $v_{\parallel} \to 0$. In this regime $v_{\perp} \simeq v_{\mathrm{th}}$, where $v_{\perp}$ is the velocity perpendicular to the magnetic field and v_{th} is the thermal velocity. Consequently, the collision frequency is almost constant and the efficiency, which only depends on $v_{\parallel}$, is high since $\eta \sim 1/v_{\parallel}$. This is the principle used in the current drive based on Alfvén waves, which have a low phase velocity. The other alternative is the high velocity case with $v_{\parallel} \gg v_{\mathrm{th}}$ and $\nu_{\mathrm{c}} \sim 1/v_{\parallel}^3$, which results in a high efficiency since $\eta \propto v_{\parallel}^2$ at large velocities. This alternative is the so-called fast electron scheme that is applied in lower hybrid current drive, where the phase velocity of the wave is high. The latter scheme is more favourable because the fast electrons are not trapped in the magnetic wells like the slower ones.

The most important question in lower hybrid current drive (LHCD) is the coupling of the waves from the launcher to the plasma. This is due to the evanescent behaviour of the waves at a density lower than the cut-off density, where $\omega^2 = \omega_{\mathrm{pe}}^2$. Especially, the coupling becomes difficult in ELMy H-mode plasmas, where the ELMs reduce the edge density strongly. The Edge Localised Modes (ELMs) peel off some of the density from the plasma, and the density in front of the antenna reduces below the cut-off density. Good coupling is very important for future devices.

In current tokamaks, a big research effort is put on so-called advanced scenarios, where the current profile is modified to get better confinement by creating transport barriers [8]. The bootstrap current, driven by a pressure gradient, has strong effect on the current profile. Of the auxiliary current drive methods, LHCD is the best candidate to modify the current profile via off-axis current drive. Neutral beams have shown off-axis power deposition, but no change in the current profile was seen [9]. Electron cyclotron current drive has also been used, but the efficiency in the main plasma phase is much worse than in LH current drive.

A problem related to the coupling of LH waves into the plasma is the generation of hot spots and impurities in the grill region. Asymmetric heat loads have been observed in LH current drive experiments on Tore Supra [10–12] and TdeV [13]. Similar observations have also been made on ASDEX [14] and JET [15]. The hot spots are strongly localised high heat loads and appear on components that are magnetically connected to the grill region, like the grill limiters or the divertor target plates. On Tore Supra, heat loads up to 10 MW/m^2 have been measured [12, 16,17] with an area of less than 10 cm^2. These heat loads are especially inconvenient

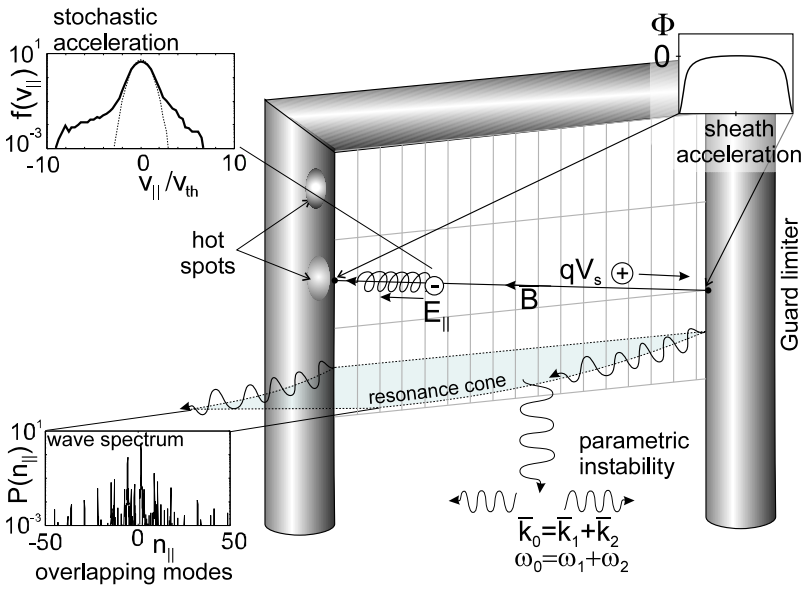

Figure 1.2: Interactions in front of the lower hybrid grill, that are the probable cause of the hot spots: the overlapping of the wave modes resulting in stochastic acceleration, as is explained in Chapter 2, and the sheath acceleration of ions. Parametric instabilities are also known to occur in front of the grill [18].

in long-pulse discharges since they limit the power level of the grill that can be used. The main topics of this thesis are the heat loads and the physics behind them.

The asymmetric power deposition on the wall structures is due to energetic particles generated in front of the LH grill. So far, there is no experimental evidence for the heat fluxes being caused by ions. Experiments on TdeV suggest that the heat fluxes are caused by energetic electrons [13] with an energy between 200 eV and 5 keV. A significant fraction of the coupled power is lost in this way. On Tore Supra, the losses are below 2%, while on TdeV they may exceed 10%. According to experiments, the loss fraction depends on the edge density and the RF power.

In Figure 1.2, some of the physical processes in front of the LH grill, possibly responsible for the hot spots, have been sketched. The figure also gives an idea of the grill structure.

A strong candidate for the hot spots and the fast electrons is the parasitic absorption of LH power [19, 20]. In parasitic absorption, the short-wavelength modes emitted by the grill are absorbed by electrons within a short distance just in front of the waveguide mouth. The modes with very high parallel refractive index, $n_{||}$, have low enough phase velocity so that the edge electrons are accelerated by the modes with $n_{||} \gtrsim 30$. Consequently a population of fast electrons is created. The

cold edge electrons ($T_e \sim 25$ eV) can reach energies up to 2 keV through stochastic acceleration in the electric field in front of the LH grill.

Other explanations for the formation of the heat load have also been given. When the electrons hit the wall, a charge separation occurs and, consequently, a sheath potential is formed. This sheath accelerates ions towards the wall structure and may therefore play a role. This mechanism has been recently studied by Tskhakaya *et al.*, see References [21–23]. Another explanation that has been studied is the so-called random fields which might enhance electron acceleration and heat fluxes [24–27]. These random-fields are spontaneously generated in front of the launcher. Thus, they make it difficult to reduce the high-$n_\parallel$ content in the spectrum by e.g. rounding off the waveguides septa as has been suggested [28]. Further analysis and a more detailed comparison between simulations and experiments are needed to confirm the mechanism behind the hot spot formation.

The development of computers has made numerical simulations a widely used tool in studying different phenomena in plasma physics and fusion research. Simulations are important tools in plasma theory development and in designing of new fusion devices. A short review of the past, present and future in computer modelling of plasmas is given in Reference [29]. One of the most popular methods of kinetic simulations of plasmas is the so-called particle-in-cell (PIC) technique [30]. In PIC codes, a spatial grid is used to describe the field quantities, while the particles may move freely in the continuous phase space. The field and particle motion are solved self-consistently, which makes the PIC simulations more realistic than pure test particle calculations where prescribed fields are used. Furthermore, the PIC codes take into account the kinetic effects of the plasma and the non-linearities of the problem. The kinetic effects are in some cases important, for instance, because the absorption of the LH power in the edge plasma generates hot electrons as was discussed earlier. Non-linear processes, such as parametric instabilities, are also known to occur in front of the LH launcher [18].

In this thesis, the use of PIC codes has been extended to a completely new branch of applications, the near-field of the LH grill. The parasitic absorption and the generation of fast electrons in front of the waveguide mouth have been explored as well as the coupling of waves from the launcher to the plasma. Usually the electron acceleration is studied with test particle simulations [17, 19] and the coupling problem with linear coupling codes [31, 32].

During the course of this work, the grill model used in the electrostatic PIC code has been developed. In the early start of our work a very simple model was used for the grill [33]. Publication I is devoted to introducing the PIC method as a tool for the fast particle generation studies. Compared to the first grill model in Reference [33] a slightly improved one is used in Publication I, though the model still is quite far from a realistic one. Some useful energy and power diagnostics are also developed in Publication I. The numerical diagnostics for both the coupled and the absorbed power is derived. The kinetic energies are obtained and the change

in the velocity distributions of the edge electrons is seen in a case with more peaks in the high-$n_{\|}$ part of the spectrum. The grill model and some of the diagnostics were also used in the study of ion Bernstein wave excitation [34, 35].

In order to get a more realistic power spectrum in the PIC simulations, the grill model was improved. The surface charge used to launch the wave in the electrostatic code is now calculated from the output of the SWAN coupling code [32]. The coupling of the PIC code XPDP2 [36] with the SWAN code is presented in Reference [37] and in Publication III. The first studies with this new grill model are presented in Reference [37], where a density study of the parasitic absorption at a fairly high temperature was carried out. The absorption seems to increase with density, though the dependence is not very strong in the density range of the simulations. A lower edge temperature is used in Publication II, where the parasitic absorption is studied for both Tore Supra and JET.

Experiments at TdeV and Tore Supra [13] indicated that the heat loads on the magnetically connected components strongly depend on the launched LH power. Therefore, in Publication III a systematic study with different power densities is performed with the PIC simulations. There are indications that the power dependence could be non-linear and, subsequently, both a linear and a non-linear scaling were derived. A comparison of the results in Reference [37] and Publication II indicate that the absorption also depends on the temperature of the edge electrons. Consequently, a study was performed to resolve this dependence. This is the main object of the second part of Publication III. The parasitic absorption clearly increases with the edge temperature, and a scaling is deduced from the proportionality to the thermal velocity. The last part of Publication III is devoted to obtaining an estimate for the heat load on the grill limiter corresponding to the parasitic absorption. Even though this estimate is just a rough one, the results agree fairly well with the experimental ones.

The studies presented in Publications II and III are for the Tore Supra LH launcher named C2, which is the older one of the two grills used at Tore Supra. Since then an improved launcher with passive waveguides between each module has been installed [38]. This antenna is called the C3. The parasitic absorption and the resulting heat loads are studied for the C3 launcher in Publication IV.

Publications I – IV show that PIC simulations are indeed a feasible method for studying the hot spot formation. The work presented in these publications clearly confirms that the cold edge electrons can be accelerated up to energies of a few keV by parasitic absorption of LH power. The simulations also show that the resulting electron flux to the walls is high enough to cause the heat loads observed on the limiters of the LH grills. The work, however, does not rule out the effect of ions because they are not considered in this work.

Publication V tackles the problem of coupling. The electromagnetic PIC codes are well enough developed so that they can be used to study the coupling from

a full-scale 32-waveguide grill to plasma. For the first time, electromagnetic PIC simulations are used to investigate the edge plasma in front of the waveguides. The advantage of the electromagnetic code is that the waveguides can be modelled more realistically. In this case, the waveguides are constructed of perfectly conducting walls, and the wave can be followed both inside the waveguides and in the plasma. Therefore, the reflection coefficients in the plasma facing waveguides can be obtained. With this new tool it is also possible to study the coupling at very low densities, close to or even below the cut-off density, where the usual approximations fail. The PIC method also enables coupling calculations with steep gradients. Such regimes have been studied in a further work, see Reference [39].

This thesis is an introduction and a review of Publications I–V. Chapter 2 describes the basic properties of the LH waves. The dielectric tensor and the dispersion relation in the cold plasma approximation are presented. Some important aspects of wave penetration and propagation are discussed as well as theories related to absorption. The chapter ends with a description of the lower hybrid grill. The basic properties of the PIC method are briefly described in Chapter 3. The grill models used in Publications I–IV are carefully explained together with some important numerical diagnostics that were developed in course of this work. The heat load estimation is also described. Chapter 4 reviews the simulation results of the studies on parasitic absorption while Chapter 5 gives an overview of the results on coupling studies made with the electromagnetic code.

Chapter 2

Lower Hybrid Waves

Lower hybrid waves at a frequency of 1–10 GHz are the most effective method to drive off-axis current in a tokamak. Unlike the ion and electron cyclotron waves, which are absorbed at the corresponding resonances, the LH waves actually have almost nothing to do with the LH resonance. In fact the launched frequency is chosen so that it is above the LH resonance frequency in the whole plasma. These waves are actually just slow plasma waves. They are not absorbed at the LH resonance, but through Landau damping. The name convention is due to historical reasons. In the early times of LH heating, a frequency below the lower hybrid resonance frequency was used. It was assumed that the power would be deposited at the LH resonance to the ions. However, the ion heating turned out to be hard to reproduce [40, 41]. Electron heating and especially current drive was found much more efficient and became more popular.

In this chapter, all aspects of waves in a cold plasma that are relevant for this work have been collected. Naturally, the emphasis is on lower hybrid waves. The first section is a review of different issues related to wave coupling and wave propagation in the plasma. The next section is devoted to wave absorption and physics related to that. Finally, the launching structure, the 'grill', is discussed at the end of the chapter.

2.1 Waves in Cold Plasmas

The wave propagation in any medium is described by the wave equation

$$\nabla \times \nabla \times \boldsymbol{E} = -\frac{1}{c^2}\frac{\partial^2 \boldsymbol{E}}{\partial t^2} - \mu_0 \frac{\partial \boldsymbol{j}}{\partial t}, \tag{2.1}$$

which is obtained by combining the Faraday and the Ampère laws, see Equations (3.3c) and (3.3d). Here, $\boldsymbol{E}$ is the electric field, c is the speed of light in vacuum, t is the time, μ_0 is the vacuum permeability, and $\boldsymbol{j}$ is the electric current density.

If the temporal and spatial dependence of the field and current density is assumed to vary as the real part of $\widehat{\boldsymbol{E}}_1 \exp\{\mathrm{i}\boldsymbol{k}\cdot\boldsymbol{r} - \mathrm{i}\omega t\}$ then, in the Fourier space the wave equation reads

$$\boldsymbol{k}\times\boldsymbol{k}\times\widehat{\boldsymbol{E}}_1 + \frac{\omega^2}{c^2}\boldsymbol{\varepsilon}\cdot\widehat{\boldsymbol{E}}_1 = 0. \tag{2.2}$$

Here, $\boldsymbol{k}$ is the wave vector, $\omega = 2\pi f$ is the angular frequency of the field and $\boldsymbol{\varepsilon}$ is the dielectric tensor. The hat denotes the Fourier space.

In writing Equation (2.2), the relation between the current density and the conductivity tensor has been used: $\widehat{\boldsymbol{j}} = \boldsymbol{\sigma}\cdot\widehat{\mathbf{E}}_1$ [42, 43]. In the cold plasma approximation, the dielectric tensor can be written as [2]

$$\boldsymbol{\varepsilon} = \mathbb{1} + i\frac{\boldsymbol{\sigma}}{\omega\epsilon_0} = \begin{pmatrix} S & iD & 0 \\ -iD & S & 0 \\ 0 & 0 & P \end{pmatrix}. \tag{2.3}$$

In the case of only one ion species, the elements S (for sum), D (for difference) and P (for plasma) are defined as [43]

$$S = 1 - \frac{\omega_{\mathrm{pe}}^2}{(\omega^2 - \Omega_{\mathrm{ce}}^2)} - \frac{\omega_{\mathrm{pi}}^2}{(\omega^2 - \Omega_{\mathrm{ci}}^2)} \tag{2.4a}$$

$$D = \frac{\omega_{\mathrm{pe}}^2\Omega_{\mathrm{ce}}}{\omega\,(\omega^2 - \Omega_{\mathrm{ce}}^2)} + \frac{\omega_{\mathrm{pi}}^2\Omega_{\mathrm{ci}}}{\omega\,(\omega^2 - \Omega_{\mathrm{ci}}^2)} \tag{2.4b}$$

$$P = 1 - \frac{\omega_{\mathrm{pe}}^2}{\omega^2} - \frac{\omega_{\mathrm{pi}}^2}{\omega^2}. \tag{2.4c}$$

Here, $\omega = 2\pi f$ is the angular frequency of the wave, and ω_{ps} and Ω_{cs} are the plasma frequency and the cyclotron frequency of particle species s, respectively:

$$\omega_{\mathrm{ps}} = \left(\frac{n_{\mathrm{s}}q_{\mathrm{s}}^2}{\epsilon_0 m_{\mathrm{s}}}\right)^{1/2} \tag{2.5}$$

$$\Omega_{\mathrm{cs}} = \frac{q_{\mathrm{s}}B_0}{m_{\mathrm{s}}}. \tag{2.6}$$

The density is denoted by n_{s}, m_{s} is the mass and q_{s} is the charge of the particle species s, ϵ_0 is the permittivity of vacuum and B_0 is the external magnetic field.

The wave equation (2.2) has a non-trivial solution if the determinant of the matrix vanishes. This condition gives the general dispersion relation. In a homogeneous or weakly inhomogeneous plasma the dispersion relation can be written in the form [43, 44]

$$An_\perp^4 - Bn_\perp^2 + C = 0. \tag{2.7}$$

Here $n_\perp = k_\perp c/\omega$ is the perpendicular refractive index, and the perpendicular and parallel components are with respect to the external magnetic field. The coefficients are

$$A = S \tag{2.8a}$$

$$B = \left(S - n_\parallel^2\right)(S + P) - D^2 \tag{2.8b}$$

$$C = P\left[\left(n_\parallel^2 - S\right)^2 - D^2\right], \tag{2.8c}$$

where $n_\parallel = k_\parallel c/\omega$ is the parallel refractive index.

Equation (2.7) has two solutions, which correspond to the slow (+) and the fast (–) waves:

$$n_\perp^2 = \frac{B \pm \left(B^2 - 4AC\right)^{1/2}}{2A}. \tag{2.9}$$

Slow and fast refer to the perpendicular phase velocities of the two modes relative to each other.[1] If the condition $B^2 = 4AC$ is satisfied, the two solutions coalesce and a mode transformation from the slow to fast mode can occur. As long as $B^2 > 4AC$, the two solutions are, however, distinct and $n_\perp$ is real, which is a requirement for the wave to propagate. In the limit, $B^2 \gg 4AC$ the two roots can be approximated as [45]

$$\text{slow wave:} \qquad n_{\perp,s}^2 \approx \frac{B}{A} \approx \frac{P}{S}\left(S - n_\parallel^2\right) - \frac{D^2}{S} \tag{2.10a}$$

$$\text{fast wave:} \qquad n_{\perp,f}^2 \approx \frac{C}{B} = \frac{D^2 - \left(n_\parallel^2 - S\right)^2}{\left(n_\parallel^2 - S\right) + D^2/P}. \tag{2.10b}$$

Equation (2.10a) gives an estimate for the radial length of the simulation box in the electromagnetic case as the box is a few perpendicular wavelengths long.

The two solutions are shown in Figure 2.1, where the roots of Equation (2.9) are presented as a function of density for the Tore Supra parameters. On the left-hand side, the whole lobes are shown for both the slow and the fast wave. The two waves are clearly distinct from each other. The right-hand side figure is just a zoom-in to lower densities. As long as $n_\perp^2$ is negative, the wave is evanescent, and when $n_\perp^2 > 0$ is reached, propagating solutions are found. From the point of view of this work, the slow wave is the more important wave. Therefore, we concentrate on the slow wave in the following discussion.

[1] The choice of sign for these two modes depends on the sign in front of the second term of Equation (2.7). In this case, the sign of the coefficient B was chosen so that it is positive for typical parameters in this work. Especially the sign of B has to be kept in mind when approximate solutions are developed as in Equations (2.10).

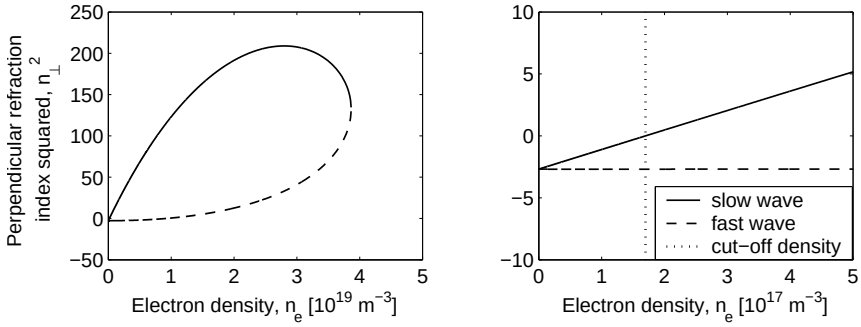

Figure 2.1: Solutions of the dispersion Equation (2.9), $n_\perp^2$ versus density ($n_e = n_i$). The parameters have been chosen for Tore Supra, i.e. $n_\parallel = 1.92$, $B = 2.78$ T and $f = 3.7$ GHz. The dashed line is the fast wave and the solid line the slow wave branch. The dotted line on the right-hand side denotes the slow wave cut-off density.

The slow wave has a *resonance* where $n_\perp \to \infty$ when $S = 0$. This is the cold plasma lower hybrid resonance having the frequency [2]

$$\omega_{\mathrm{LH}}^2 = \omega_{\mathrm{pi}}^2 \left[1 + \frac{\omega_{\mathrm{pe}}^2}{\Omega_{\mathrm{ce}}^2} \right]^{-1} . \tag{2.11}$$

The density at which the resonance occurs for a given magnetic field and frequency can easily be solved from this equation by taking $\omega = \omega_{\mathrm{LH}}$. A fairly simple equation is given in Reference [2, p. 263].

Another special point occurs when $n_\perp = 0$. This layer is called the *cut-off*. At this point the propagating wave with $n_\perp > 0$ is changed into an evanescent one with $n_\perp < 0$, or vice versa. At the cut-off, the phase velocity of the wave $v_{\mathrm{ph}} = \omega/k$ approaches infinity, and the wave is reflected. From Equation (2.7) it is seen that the cut-off with $n_\perp = 0$ occurs at $C = 0$, i.e. at $P = 0$ or ${n_\parallel}^2 = S + D$, as is seen from Equation (2.8c). In the right-hand side frame of Figure 2.1, which shows the dispersion curve around the slow wave cut-off, the cut-off at $n_e = 1.66 \times 10^{17}$ m^{-3} is denoted by the dotted line.

For the lower hybrid range of frequencies, the more important cut-off is the one coming from $P = 0$. This is the plasma wave cut-off at which the cut-off frequency is $\omega = \omega_{\mathrm{pe}}$. This equation determines the cut-off density. Below this density the wave can not propagate. However, if the evanescent layer is narrow enough, part of the wave power can reach the region of higher density where it can propagate. Naturally, the densities in the simulations have been chosen above the slow wave cut-off density.

Another criterion for the propagation of the wave is obtained from the inequality $B^2 - 4AC > 0$ for the discriminant in Equation (2.9). This is the condition that the wave does not face a mode transformation region. If the frequency of the wave

is above the lower hybrid resonance frequency, $\omega > \omega_{\mathrm{LH}}$, this criterion, called the Stix-Golant accessibility condition, is [43, 45]

$$n_{\parallel \mathrm{crit}}^2 > \left(\sqrt{S} + \frac{D}{|P|} \right)^2 . \tag{2.12}$$

If the lower hybrid resonance is present in the plasma then this criterion reads

$$n_\parallel^2 > 1 + \left. \frac{\omega_{\mathrm{pe}}^2}{\Omega_{\mathrm{ce}}^2} \right|_{\omega=\omega_{\mathrm{LH}}} . \tag{2.13}$$

Far from the resonance, the electrostatic approximation of the cold plasma dispersion relation can be used. This approximation is widely used in wave and instability calculations since it allows the use of scalar equations instead of vector equations. The approximation is simply $\boldsymbol{E} = -\nabla\phi$, resulting in $\boldsymbol{k} \cdot \boldsymbol{\varepsilon} \cdot \boldsymbol{k} = 0$ from Equation (2.2). Consequently, the cold plasma dispersion relation reads [43]

$$\epsilon = k_\perp^2 S + k_\parallel^2 P = 0. \tag{2.14}$$

In the electrostatic approximation the electric field and the wave vector point in the same direction. This holds very well for the modes with large refraction index $n_\parallel^2 \gg 1$, which in fact is the range of interest in most of this work. The electrostatic cold plasma dispersion relation can also be obtained from Equations (2.7) and (2.8) in the limit $S \approx 1,\ D^2 \ll 1$ and $|P| \gg 1$. The electrostatic dispersion relation is used to determine the length of the simulation box in the electrostatic case. The radial length of the simulation box is a few perpendicular wavelengths, where the wavelength is calculated at the low-density edge.

When the wave is excited from the source, the power is not radiated into all spatial directions. More likely, the field is concentrated in conical structures called *resonance* or *propagation cones*. This was first shown theoretically by Kuehl [46] for a point source and then experimentally by Fisher and Gould [47, 48], who called this structure of singular lines a resonance cone. Briggs and Parker [49] showed experimentally that the lower hybrid waves propagate in resonance cones. Bellan and Porkolab showed both theoretically and experimentally [50] that a source of finite dimensions and periodic structure excites waves that propagate in such cones. These cones are also seen in the PIC simulations of this work.

The trajectories of the resonance cones can be derived from the cold plasma dispersion relation. Strictly speaking the derivation should go through the Fourier transformation of the relation, but a much easier way leading to the correct result is obtained from the dispersion relation in the form $\nabla \cdot \boldsymbol{\varepsilon} \cdot \nabla\phi = 0$ [50]. In the following consideration, a 2D slab geometry is assumed. The magnetic field is along the z-direction and the density grows in the x-direction. In a homogenous or weakly inhomogeneous cold plasma this dispersion relation becomes

$$\frac{\partial^2 \phi}{\partial x^2} = -\frac{P}{S} \frac{\partial^2 \phi}{\partial z^2}, \tag{2.15}$$

which has the solutions propagating along the characteristics $z \pm x \left(-P/S\right)^{1/2}$. The cones can thus be calculated from the equation

$$z(x) = z_0 \pm x \left(\frac{-P}{S}\right)^{1/2}, \tag{2.16}$$

where $z_0 = z(x = 0)$ is the z co-ordinate at the starting point of the wave.

The wave packet propagates in the cones with the group velocity $\boldsymbol{v}_\mathrm{g}$, which can be obtained from the dispersion relation [51]

$$\boldsymbol{v}_\mathrm{g} = \frac{\partial \omega}{\partial \boldsymbol{k}} = \left.\frac{\partial \omega}{\partial k_\perp}\right|_{k_\parallel} \hat{\mathbf{e}}_\perp + \left.\frac{\partial \omega}{\partial k_\parallel}\right|_{k_\perp} \hat{\mathbf{e}}_\parallel. \tag{2.17}$$

Here, the notation $|_{k_\parallel}$ means that $k_\parallel$ is assumes fixed, and respectively for $k_\perp$. For the perpendicular and parallel group velocities, the equations read [7, 51]

$$v_{g,\perp} = \left.\frac{\partial \omega}{\partial k_\perp}\right|_{k_\parallel} = -\left.\frac{\partial \epsilon / \partial k_\perp}{\partial \epsilon / \partial \omega}\right|_{k_\parallel} = -\frac{k_\perp}{k_\parallel^2}\frac{S}{\alpha} \tag{2.18a}$$

$$v_{g,\parallel} = \left.\frac{\partial \omega}{\partial k_\parallel}\right|_{k_\perp} = -\left.\frac{\partial \epsilon / \partial k_\parallel}{\partial \epsilon / \partial \omega}\right|_{k_\perp} = -\frac{1}{k_\parallel}\frac{P}{\alpha} \tag{2.18b}$$

$$\alpha = \omega \left\{ \frac{\left(\omega_\mathrm{pe}^2 + \omega_\mathrm{pi}^2\right)}{\omega^4} - \frac{P}{S}\left[\frac{\omega_\mathrm{pe}^2}{\left(\omega^2 - \Omega_\mathrm{ce}^2\right)^2} + \frac{\omega_\mathrm{pi}^2}{\left(\omega^2 - \Omega_\mathrm{ci}^2\right)^2}\right]\right\}, \tag{2.18c}$$

where $\epsilon\left(\omega, k_\perp, k_\parallel\right)$ is the dielectric response function given in Equation (2.14). The perpendicular wave number $k_\perp$ is obtained from the cold plasma dispersion relation and the sign has to be chosen so that the perpendicular group velocity is positive, i.e. $k_\perp < 0$ since S and α are positive. Note also that the sign of the parallel group velocity depends only on $k_\parallel$ since P is negative, i.e. $v_{g,\parallel} = |P| / (k_\parallel \alpha)$. In the limit $\Omega_\mathrm{ci}^2 \ll \omega^2 \ll \Omega_\mathrm{ce}^2$ and using $\omega_\mathrm{pi}^2 \ll \omega_\mathrm{pe}^2$ the coefficient α is reduced to

$$\alpha \approx \omega \left\{ \frac{\omega_\mathrm{pe}^2}{\omega^4} - \frac{P}{S}\left[\frac{\omega_\mathrm{pe}^2}{\Omega_\mathrm{ce}^4} + \frac{\omega_\mathrm{pi}^2}{\omega^4}\right]\right\}. \tag{2.19}$$

The group velocity is used to determine the simulation length in the electrostatic case. The simulation is stopped when the wave is expected to reach the high-density boundary. Together with the energy density of the wave the group velocity is also used to calculate the power densities. The phase velocity in the two directions is obtained from

$$v_{\mathrm{ph},\perp} = \frac{\omega}{k_\perp} \tag{2.20a}$$

$$v_{\mathrm{ph},\parallel} = \frac{\omega}{k_\parallel}. \tag{2.20b}$$

Comparing Equations (2.18) and (2.20), we notice that the cold plasma wave is a 'backward' wave in the perpendicular direction. In this context, backward means

that the phase velocity and the group velocity are in opposite directions. In the perpendicular direction, $k_\perp < 0$ has to be chosen in order for the wave to propagate from the edge into the plasma, i.e. to have $v_{g,\perp} > 0$. Subsequently, the perpendicular phase velocity is negative. In the parallel direction, both the group and the phase velocity have the same sign as $k_\parallel$ since $P < 0$. Consequently, the wave is a 'forward' propagating wave in this direction.

2.2 Quasilinear Absorption

The absorption of the wave by the plasma is through a resonant interaction between the wave and the particles. This interaction is called Landau damping [43, 52]. In Landau damping, the particles that have a velocity close to the phase velocity of the wave interact with the wave [42, 43, 52]. In the velocity distribution the particles that are slightly faster than the phase velocity of the wave loose energy and those that are somewhat slower gain energy. Since usually the population of faster particles is clearly smaller than that of the slower ones, the particles tend to gain energy rather than loose. Consequently, the wave looses energy and is damped. The first experimental evidence of Landau damping was presented by Malmberg and Wharton [53].

In a magnetised plasma, the Landau damping involves electrons having the parallel velocity close to the parallel phase velocity of the waves $v_{\mathrm{ph},\parallel} = \omega/k_\parallel$. The damping rate is proportional to the gradient of the velocity distribution, i.e. $\gamma_\mathrm{e} \sim \partial f(v_\parallel)/\partial v_\parallel$. When the slightly slower particles ($v \lesssim \omega/k_\parallel$) are accelerated and the slightly faster ones ($v \gtrsim \omega/k_\parallel$) decelerated, a plateau is formed in the initially Maxwellian distribution. As long as there are more slower particles than faster ones, $\gamma_\mathrm{e} < 0$ and the wave is damped.

The Landau damping rate can be approximated by [54]

$$\gamma_\mathrm{e} = -\sqrt{\pi}\frac{\omega^2\omega_\mathrm{pe}^2}{k^2 k_\parallel v_\mathrm{the}^3}\exp\left(-\frac{v_{\mathrm{ph},\parallel}^2}{v_\mathrm{the}^2}\right) \tag{2.21}$$

where $k^2 = k_\perp^2 + k_\parallel^2$ and $v_\mathrm{the} = (2k_\mathrm{B}T_\mathrm{e}/m_\mathrm{e})^{1/2}$. The damping length is then obtained as

$$L_\gamma = \frac{v_{g,\perp}}{\gamma_\mathrm{e}}. \tag{2.22}$$

The previous equations are valid as long as the electron Larmor radius is much smaller than the smallest wavelength of interest, i.e. $r_\mathrm{L,e} = v_\mathrm{the}/\Omega_\mathrm{e} \ll \lambda_\mathrm{min}$, the temperature is isotropic, and $\left|\omega/(k_\parallel v_\mathrm{the})\right|$ is large. The damping rate obtained from these equations can be compared to the ones from the simulations.

The damping is strong if the phase velocity of the wave is of the order of the electron thermal velocity, i.e. $v_{\mathrm{ph},\parallel} = \omega/k_\parallel \sim \mathcal{O}(v_\mathrm{the})$ [55]. This was also described to hold

for perpendicular ion motion [56, 57], though the ions need to have a very large energy in order to fulfil the requirement of $v_{\mathrm{ph},\perp} \sim \mathcal{O}(v_{\mathrm{thi}})$. The smallest parallel refractive index participating in the absorption to electrons at a given temperature is given by [40, 58, 59]

$$n_{\parallel} \gtrsim \frac{5.8}{\sqrt{T_{\mathrm{e}}\,(\mathrm{keV})}} \tag{2.23a}$$

$$n_{\parallel} \gtrsim \frac{7.0}{\sqrt{T_{\mathrm{e}}\,(\mathrm{keV})}}, \tag{2.23b}$$

where the first equation is for the case of linear Landau damping and the second one is for the quasi-linear case once the plateau at the phase velocity is formed. These equations, together with the Stix-Golant condition Equation (2.12), indicate that it is almost impossible for the LH wave to penetrate into the centre of the plasma but it will be absorbed further outside. For a 1 keV plasma, as in Publication V, the modes $n_{\parallel} \gtrsim 5.8$ are absorbed. This is also seen in the simulations. In a plasma with a higher temperature of $T_{\mathrm{e}} = 10$ keV, the absorption starts already for the mode $n_{\parallel}$=1.8.

The particles moving with a velocity close to the phase velocity feel also another force. They feel the potential structure of the wave. Particles moving close enough to the phase velocity of the wave do not have enough energy to overcome the potential well of the wave. They are therefore called trapped particles [18, 51]. Other particles that have more energy may move untrapped, though they feel the potential slightly if they are not too energetic. The trapping width, or the trapping velocity, separating the two regions, the trapped and untrapped, is obtained in the velocity space for the Fourier mode as

$$v_{\mathrm{tr}} = 2\left|\frac{q_{\mathrm{e}}\widehat{E}_{k_{\parallel}}}{m_{\mathrm{e}}k_{\parallel}}\right|^{1/2}. \tag{2.24}$$

The electrostatic trapping is illustrated in Figure 2.2.

The overlapping of the trapping widths of the different modes in the Chirikov sense [60] can enhance the acceleration of the electrons remarkably. When the modes overlap, the particles in the potential well of one mode can stochastically move to the well of the next mode [19]. This is illustrated in Figure 2.3. The motion is stochastic in the sense that it is impossible to predict the trajectory of the electrons in the velocity space. The electrons first interact resonantly with the high-$n_{\parallel}$ modes having a low phase velocity. At high power levels, the particles can then move stochastically in the region of overlapping trapping widths towards higher energies. They reach phase velocities of lower and lower $n_{\parallel}$ modes and gain energy as long as the modes overlap. Through this stochastic acceleration the cold ($T_{\mathrm{e}} \sim 25$ eV) electrons may reach energies up to 2 keV. This upper limit is due to the large energy gap between the first two forward-propagating modes [19]. Consequently, the overlapping also broadens the plateau in the velocity space.

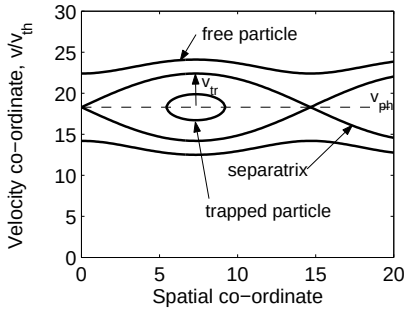

Figure 2.2: Trajectories of trapped and untrapped particles, as well as the separatrix. Here the spatial co-ordinate is moving at the phase velocity. The dashed line denotes the phase velocity of the wave.

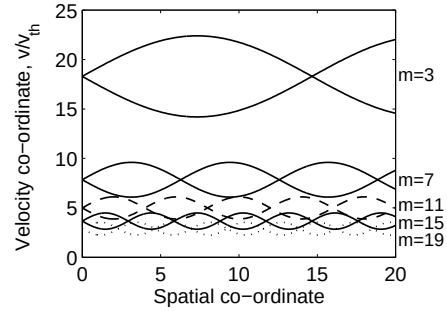

Figure 2.3: Overlapping of trapping widths for modes shown on the right. The trajectories are calculated according to Equation. (12) in Reference [19] with amplitude of electric field $E_0 = 3$ kV/cm and $T_e = 25$ eV. The spatial co-ordinate is Ω_m/k_m, where $0 < \Omega_m < 18\pi$ and k_m is the wave number of mode m.

The absorption of the wave power and the stochastic acceleration modify the originally Maxwellian velocity distribution. The time scale at which the hot tail in the velocity distribution is generated is determined by the so-called quasilinear diffusion time [18, 61]

$$\tau_{\mathrm{QL}} = \frac{v_{\mathrm{the}}^2}{D_{\mathrm{QL}}}, \quad \text{where} \quad D_{\mathrm{QL}} = \frac{\pi q_e^2 k_\parallel}{2 m_e^2 \Delta v_{\mathrm{ph},\parallel}} \left|\widehat{\phi}\right|^2 . \tag{2.25}$$

Here, D_{QL} is the quasilinear diffusion coefficient in velocity space and the spacing between the resonant velocities is $\Delta v_{\mathrm{ph},\parallel} = \left| v_\parallel - v_{\mathrm{g},\parallel}(k_\parallel) \right| \Delta k_\parallel / k_\parallel$, where $v_{\mathrm{g},\parallel}$ is the group velocity and $\Delta k_\parallel = 2\pi/L$. The width of the grill is L. A well-developed tail in the distribution function is obtained in a few quasilinear diffusion times. Therefore, the simulations should extend over at least a few diffusion times.

2.3 Lower Hybrid Grill

The use of a phased waveguide array for launching lower hybrid waves into the plasma was first suggested by Lallia [62]. Due to the similarity to the cooking utensil, the device is called a grill. The grill consists of an array of properly phased waveguides. Klystrons are used to feed the waveguides with a transverse electric (TE_{10}) mode. For current drive, the phasing between adjacent waveguides in a row should be $\pi/2$ or $\pi/3$ in order to get an asymmetric wave spectrum. First, it was thought that the rows, i.e. the vertically adjacent waveguides, should be in phase, but later it has been shown that this is not compulsory. The poloidal wave number seems to have no effect on absorption.

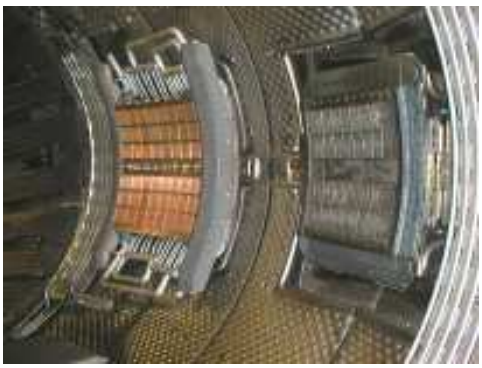

Figure 2.4: The two LH antennae of Tore Supra.

The advantage of a grill as a launching structure is that the wave source can be far behind the mouth. The waves are then transmitted to the plasma facing structure through waveguides. The vacuum area inside the plasma chamber is separated by a dielectric window from the pressurised area outside it. This window can be placed far away from the plasma thus reducing the heat and neutron fluxes on it. Moreover, the grill can, in principle, be made of the same material as the wall or the poloidal limiters, in front of which it usually is not moved. However, the inner part of the grill has to be made of copper to ensure good RF conductivity.

In a large tokamak, a conventional LH grill made of independently fed waveguides would need a few hundred or even thousands of waveguides. This would make the grill structure very complex and demanding to design. Therefore, the use of multijunction grills was suggested [63, 64]. In a multijunction grill, the main waveguide is divided into smaller, secondary waveguides with metal walls parallel to the wall of the main waveguide. The height of the secondary waveguides is chosen so that the correct output phasing is obtained for the grill [65].

The main waveguide, in a multijunction grill, is again fed with the TE_{10} mode. Further inside the waveguides, this mode is converted into a TE_{30} mode in poloidal mode converters. H (magnetic field) and E (electric field) plane junctions are used to divide the power in the incident waveguides into poloidal and toroidal multijunctions. Due to the division into three in the poloidal direction, it is actually a TE_{10} mode that reaches the grill mouth [66].

Figure 2.4 shows the plasma facing parts of the two grill generations used at Tore Supra. The older grill, called C2, is on the right-hand side and the newer one, called C3, is on the left-hand side. The waveguide rows and mouths can be seen as well as the limiters.

The C2 antenna is constructed of 4 rows each having 32 waveguides [66, 67]. The waveguides are divided into modules consisting of two rows of four waveguides. In

the multijunction structure, the toroidal phase difference is $\pi/2$ between adjacent waveguides in a module. In addition, there is a phase shift between the modules. This phase shift can be varied from 0 up to 2π. A zero phase difference between the modules results in $\pi/2$ phase difference between each waveguide. This is the more favourable case for current drive because it optimises the directivity and the self-matching properties of the multijunction [68].

The C3 grill is made of 48×6 waveguides [68, 69]. In addition, passive waveguides are used between each module and at both ends of the launcher. Unlike active waveguides the passive ones are not fed by klystrons. For the same input power, the larger radiating surface in the C3 launcher results in a lower coupled power density of $I_{\mathrm{in}} = 25$ MW/m^2 at 3.7 GHz. The decreased power density allows driving current in long pulses since it helps to avoid for example RF-breakdowns.

In the next generation launcher, even more passive waveguides are used. The design of the LH grill of ITER is based on Passive Active Multijunctions (PAM), which allow good coupling of the wave and efficient cooling of the plasma facing part of the grill [70,71]. The whole grill is constructed of four PAM modules. Each module consists of 12 rows of 24 active and 25 passive waveguides in a row [71]. The phase difference between adjacent active waveguides in the row is $3\pi/2$. Preliminary tests on such a grill have been made and tests on plasma are foreseen in the beginning of 2003 [72].

The spectrum of the wave launched by the grill is determined by the dimensions and the frequency of the launcher together with the phase difference between the radiating waveguides. The main peak carrying most of the power can be found from the equation [58]

$$n_{\|0} = \frac{\lambda_0}{\Delta z}\frac{\Delta\varphi}{2\pi}. \tag{2.26}$$

Here, $\lambda_0 = c/f$ is the vacuum wavelength of the driven wave, Δz is the width of the geometric period of the grill and $\Delta\varphi$ is the phase difference between two radiating elements. The geometric period means the width of the waveguide including the wall between the two adjacent waveguides. For a PAM module the passive waveguide with its wall has also to be included.

In a simple multijunction with a phase difference of $\Delta\varphi = \pi/2$, the positions of the peaks can be obtained from the formula

$$n_{\|m} = \frac{c}{fL_4}m. \tag{2.27}$$

Here, m is the mode number and L_4 is the shortest period of the grill, i.e. the width of 4 waveguides. For the $\pi/2$ phasing, the spectrum is asymmetric with only the odd harmonics present [19]. The even ones are suppressed. Consequently, the mode number is $m = 1 \pm 4\sigma$, with $\sigma = 1, 2, 3, \ldots$ Moreover, the wave modes $m = 1, 5, 9$, etc. propagate toroidally in one direction while the modes $m = -3, -7, -11, \ldots$ propagate in the opposite direction. The modes $m = 1, 5, \ldots$ are sometimes referred

as forward-propagating modes and the ones with $m = -3, -7, \ldots$ as backward ones. This naming only refers to the propagation in the toroidal direction with respect to the principal mode and has nothing to do with the backward wave discussed in the previous section.

The half width of the peak is also determined by the geometry of the grill. The width is inversely proportional to the toroidal width of the launcher [73]

$$\Delta n_{\parallel} = \frac{c}{\omega} \frac{2\pi}{L_{\mathrm{G}}} = \frac{c}{f L_{\mathrm{G}}}. \tag{2.28}$$

Here, $\Delta n_{\parallel}$ denotes the full width at half maximum and L_{G} is the full width of the grill. For a passive active multijunction, $L_{\mathrm{G}} = N d_{\mathrm{act}}$ is the width of the actively radiating part of the grill, where N is the number and d_{act} is the width of the active waveguides. The width of the peak is an important parameter in the current drive efficiency, which increases for a smaller width of the main peak. This is the reason for using wider grills in current tokamaks. The peak in a 32-wageuide grill is much narrower than in a 4-waveguide one. Consequently, the current drive efficiency is also much better in the present day devices than in the early ones.

Chapter 3

Particle-in-Cell Model of a Lower Hybrid Grill

Particle simulations have become a widely used tool in both magnetically and inertially confined fusion plasmas. The simulations are also used for space plasmas, microwave devices, etc. [30]. However, particle-in-cell (PIC) simulations are not so widely used in fusion plasma studies. In this work, the PIC method is for the first time applied to simulations of the near field of the lower hybrid grill and parasitic absorption of the LH power.

In this chapter, the various models used in Publications I–IV are discussed. First, the particle-in-cell method is described in general. Then the grill models used in the electrostatic part of the work are discussed. We start with the simplest model used in Publication I and continue with the more sophisticated one used in Publications II–IV. At the end of the chapter, an estimate for the heat load on the grill limiter is derived.

3.1 Basic Properties of PIC Method

In the particle-in-cell method [30], particles are treated as elements of charge. The particles are loaded in the continuous $\boldsymbol{x}, \boldsymbol{v}$ phase space in the beginning of the simulation while the fields are represented on a discrete grid. The basic equations are the equations of motion, which are solved for each particle:

$$m\frac{d\boldsymbol{v}}{dt} = q\left(\boldsymbol{E} + \boldsymbol{v} \times \boldsymbol{B}\right) \tag{3.1a}$$

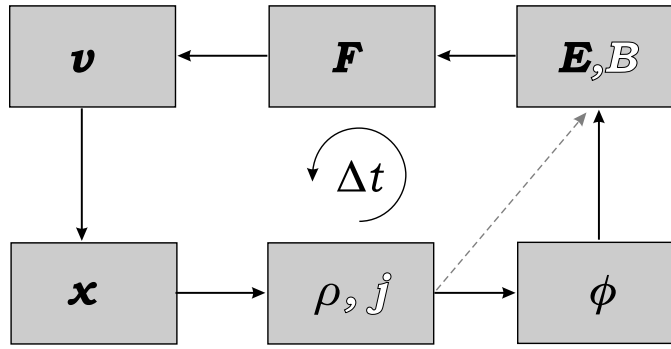

Figure 3.1: The time step of a particle-in-cell simulation. The white letters and the arrow with broken line refer to the electromagnetic code.

$$\frac{d\boldsymbol{x}}{dt} = \boldsymbol{v}, \tag{3.1b}$$

where m is the mass of the particles, $\boldsymbol{v}$ is the velocity, q is the charge, $\boldsymbol{E}$ and $\boldsymbol{B}$ are the electric and magnetic fields, respectively, and $\boldsymbol{x}$ is the position of the particle.

In the electrostatic (ES) case, the electric field $\boldsymbol{E} = -\nabla\phi$ is obtained from the Poisson equation

$$\nabla^2\phi = -\frac{\rho}{\epsilon_0}, \tag{3.2}$$

where ϕ is the electrostatic potential and ρ is the charge density. The static magnetic field in the Lorentz force is an externally applied one and is not calculated in the ES approximation. The electrostatic approximation is valid for lower hybrid waves with large values of the parallel refractive index $n_\parallel$, which is the most important parameter region in this work.

In electromagnetic (EM) particle-in-cell codes, the complete set of Maxwell's equations is solved to obtain both the electric and the magnetic field

$$\nabla \cdot \boldsymbol{E} = \frac{\rho}{\epsilon_0} \tag{3.3a}$$

$$\nabla \cdot \boldsymbol{B} = 0 \tag{3.3b}$$

$$\nabla \times \boldsymbol{E} = -\frac{\partial \boldsymbol{B}}{\partial t} \tag{3.3c}$$

$$\nabla \times \boldsymbol{B} = \mu_0 \boldsymbol{j} + \frac{1}{c^2}\frac{\partial \boldsymbol{E}}{\partial t}. \tag{3.3d}$$

The source terms in both cases are obtained from the particle data. The charge density ρ on the grid is calculated by splitting the charge of the particles to the nearest grid points e.g. by linear interpolation. In the EM case, the current density $\boldsymbol{j}$ is obtained from the positions and velocities of the particles.

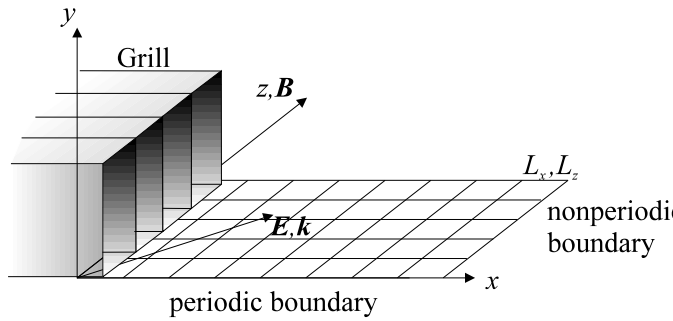

Figure 3.2: The simulation geometry in the electrostatic case (Publication I).

Figure 3.1 shows a time step of a particle-in-cell simulation. The positions and velocities of the particles are used to calculate the source terms, ρ and $\boldsymbol{j}$, which are interpolated to the grid. They are then used in either the Poisson equation in the ES case or the Maxwell equations in the EM case, to obtain the updated values of the self-consistent fields. From the fields, the Lorentz force is calculated and interpolated back to the positions of the particles. Thereafter, the equations of motion are solved to obtain the new values of the velocities and positions. For more details on the algorithms, see References [30, 36, 74]

The electrostatic PIC code XPDP2 [30, 36] used in this work is two-dimensional in configuration space and three-dimensional in velocity space. The boundary conditions are periodic in the toroidal z direction and bounded in the radial x direction. The two-dimensional slab geometry of the simulation is illustrated in Figure 3.2. The electrostatic field and the wave vector lie in the x, z plane and the static magnetic field is along the periodic z axis. The grill mouth is also along the toroidal z axis and the wave is launched from the grill in the radial x direction. In the poloidal y direction, the waveguides are assumed to be infinite. The geometry of the electromagnetic simulations and the code XOOPIC [74] will be discussed in Section 5.1.

3.2 Phenomenological Grill Model

In the electrostatic PIC codes, the grill is modelled with an external oscillating charge density [75, 76]. The first study on fast particle generation by LH waves near the grill was presented in Reference [33]. In this work, the grill was modelled with a sinusoidally oscillating charge density $\rho_{\text{ext}} = \rho_0 \delta\left(x - x_{\text{ext}}\right) \sin\left(\omega t - n\Delta\varphi\right)$. Here, ρ_0 is the amplitude of the antenna, $n = 0, 1, 2, \ldots, N-1$, where N is the number of waveguides, $\Delta\varphi$ is the phase difference between adjacent waveguides and $\omega = 2\pi f$ is the angular frequency of the grill. A phase difference of $\Delta\varphi = \pi/2$ and a frequency of $f = 3.7$ GHz were used.

In this first study, the plasma edge density was $n_{\mathrm{e,i}} = 3 \times 10^{18}$ m^{-3} and the edge temperature was $T_{\mathrm{e,i}} = 100$ eV. A mass ration of $m_{\mathrm{i}}/m_{\mathrm{e}} = 100$ was used in order to speed up the ions.

A clear distortion in the velocity distribution of the bulk electrons was seen at the phase velocity of the mode close to $n_{\parallel} \approx 18$. A rapid increase in the parallel velocity of test electrons was also clearly observed. With test particles we mean particles that do not contribute to the field calculation but are there only for the purpose of diagnostics. Their kinetic energy increased by 30% in a short time of just slightly over 5 ns. Similar results were also reported in Reference [77], where the average parallel kinetic energy in front of the grill rose by 100 % in just 2 ns.

The first model described above contains only a small amount of power in the higher harmonics. In order to study the effect of the short-wavelength modes on the electron acceleration, a slightly modified grill model was needed. In the early study of Publication I, the following approximation was used

$$\rho_{ext} = \rho_0 \left(1 + \epsilon \left| \frac{z - z_n}{b_n} \right|^{\mu} \right) \sin\left(\omega t - n\Delta\phi\right) \delta(x - x_{\mathrm{ext}}). \tag{3.4}$$

Here ρ_0 is the amplitude, ϵ and μ are constants determining the peakedness of the charge near the wall of a waveguide, z_n is the toroidal z coordinate in the middle on the n^{th} waveguide, $2b_n$ is the width of the n^{th} waveguide and $\Delta\phi = -\pi/2$ is the phase difference between the waveguides. The surface charge is located at the plane $x = x_{\mathrm{ext}}$ in the radial direction. The parameters used for the simulations with the phenomenological grill are given in Table I of Publication I.

The charge density resulting from Equation (3.4) is shown in Figure 3.3. Figure 3.3(a) shows the charge density with the parameters $\epsilon = 3$ and $\mu = 4$. This charge density is very peaked to the waveguide walls. Consequently, there is much more power in the high-$n_{\parallel}$ part of the spectrum. Figure 3.3(b) shows the charge density with $\epsilon = \mu = 0$, which is flat inside the waveguides. This one corresponds to the very first charge density model used in References [33, 77], with a low power content in the short-wavelength modes.

The power coupled to the plasma can be calculated from the change in the kinetic and electrostatic energy during the simulation. Assuming that no energy is lost, all the coupled energy is either in the kinetic energy of the electrons or ions, or in the electrostatic field energy. Consequently, the coupled power per unit length in the radial direction averaged over the time $\Delta\tau$ is calculated from the energies as

$$P_{\mathrm{in}}(x) = \frac{\Delta E_{\mathrm{kin,e}} + \Delta E_{\mathrm{kin,i}} + \Delta W_{\mathrm{ES}}}{\Delta\tau \Delta x}. \tag{3.5}$$

The change in the kinetic energy of the electrons and ions in the interval $x - \Delta x/2 \leq x \leq x + \Delta x/2$ in time $\Delta\tau$ is denoted by $\Delta E_{\mathrm{kin,e}}$ and $\Delta E_{\mathrm{kin,i}}$, respectively. The change in the electrostatic energy is approximately equal to the electrostatic energy of the wave, $\Delta W_{\mathrm{ES}} \simeq W_{\mathrm{ES}}$ because there is no wave in the beginning of the

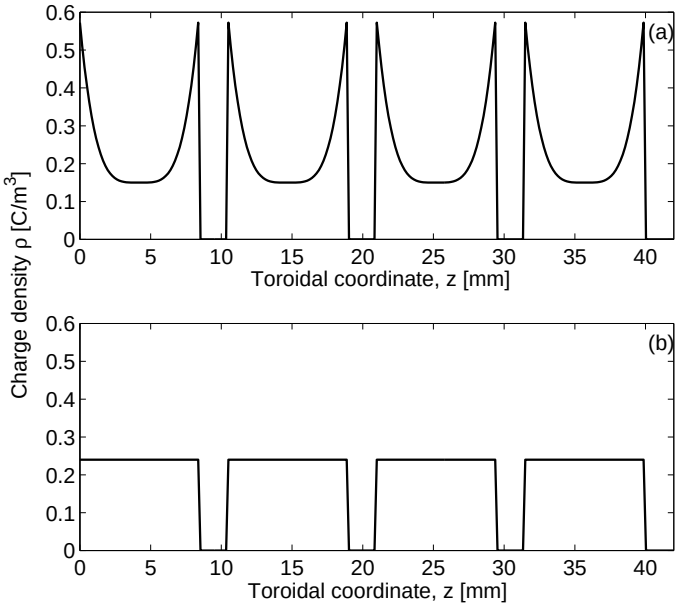

Figure 3.3: The amplitude of the charge density used in the phenomenological model for (a) the high-$n_\parallel$ simulation and (b) the reference simulation (Publication I).

simulation. The coupled power density per unit length is obtained by dividing the coupled power by the area of the grill, $I_{\mathrm{in}}(x) = P_{\mathrm{in}}(x)/A$.

The amount of power absorbed by the electrons per unit length is calculated as

$$P_{\mathrm{abs,e}}(x) = \frac{\Delta E_{\mathrm{kin,e}} - \Delta W_{\mathrm{kin,e}}}{\Delta\tau \Delta x}, \tag{3.6}$$

where $\Delta W_{\mathrm{kin,e}} \simeq W_{\mathrm{kin,e}}$ is the change in the kinetic energy density of the electrons in the time interval $\Delta\tau$ due to their oscillation with the wave. The energy due to the oscillation is obtained from the linear theory, where the oscillation velocities are calculated with the aid of the cold plasma conductivity tensor:

$$W_{\mathrm{kin,e}}(x) = \frac{\epsilon_0}{8}\left[\left(\frac{\omega_{\mathrm{pe}}^2\left(\omega^2+\omega_{\mathrm{ce}}^2\right)}{\left(\omega^2-\omega_{\mathrm{ce}}^2\right)^2}\right)E_x^2 + \left(\frac{\omega_{\mathrm{pe}}^2}{\omega^2}\right)E_z^2\right]. \tag{3.7}$$

The ion energies could be obtained in a similar manner but they are negligible compared to the electron energies.

The absorbed power density profiles are shown in Figure 3.4 for the two cases: the one with slightly more power in the high-$n_\parallel$ part of the spectrum and the reference case with $\epsilon = \mu = 0$ in Equation (3.4). The high-$n_\parallel$ case is shown in the upper frame and the one with less power in the short-wavelength modes is shown in the lower frame. As is expected, the absorption is very peaked to the edge as most of

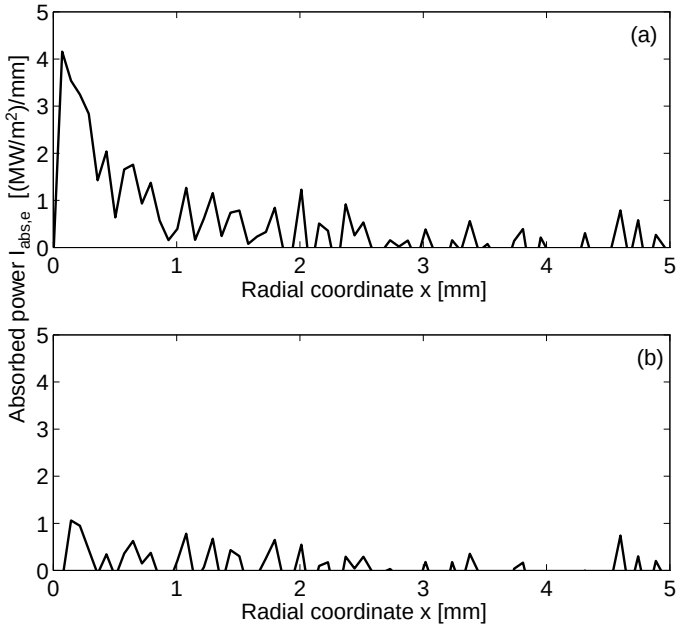

Figure 3.4: Absorbed power density versus radial co-ordinate in the simulations with the phenomenological grill model for (a) the high-$n_\parallel$ simulation and (b) the reference simulation (Publication I).

the absorption takes place within the first millimetre in front of the grill. About 5% of the coupled power is absorbed within 1.7 mm. In the reference case, hardly any absorption can be seen. In this case, only 1% is absorbed within the 1.7 mm.

The absorption is also seen in the velocity distributions. In the velocity distribution of the high-$n_\parallel$ case, a clear broadening is seen around 3 or 4 thermal velocities just in front of the grill. The phase velocity of the mode $n_\parallel$=15 corresponds to $v_{\mathrm{ph}} \approx 3.4 v_{\mathrm{e}}$. Further inside the plasma, the hot tail disappears. In the reference case, hardly any change is observed compared to the initial Maxwellian distribution. The distributions are shown in Figures 10 and 11 of Publication I.

The spectrum of the launched power is obtained in the electrostatic approximation from the group velocity and the energy density of the wave mode as

$$S(n_\parallel) = v_{\mathrm{g},\perp,\mathrm{n}_\parallel} W_{n_\parallel} \tag{3.8a}$$

$$v_{\mathrm{g},\perp,\mathrm{n}_\parallel} = -\frac{c}{n_\parallel} \left(-PS\right)^{1/2} \frac{1}{\alpha} \tag{3.8b}$$

$$W_{n_\parallel} = \frac{1}{2}\epsilon_0 \left|\widehat{E}_z\left(x, n_\parallel\right)\right|^2 \alpha \tag{3.8c}$$

$$\alpha = \frac{\omega_{\mathrm{pe}}^2 + \omega_{\mathrm{pi}}^2}{\omega^2} - \frac{P}{S}\omega^2 \left(\frac{\omega_{\mathrm{pe}}^2}{\left(\omega^2 - \omega_{\mathrm{ce}}^2\right)^2} + \frac{\omega_{\mathrm{pi}}^2}{\left(\omega^2 - \omega_{\mathrm{ci}}^2\right)^2} \right). \tag{3.8d}$$

Here, $\widehat{E}_z\left(x, n_\parallel\right)$ is the Fourier transform of the toroidal electric field. The spectra obtained from the simulations with the phenomenological grill are shown in Figures 3 and 4 of Publication I. The difference in the high-$n_\parallel$ part of the spectra is clear.

3.3 Refined Model by Coupling to SWAN

In order to model experiments with a more realistic wave spectra, XPDP2 was coupled with the SWAN code [32]. The Slow Wave ANtenna code SWAN, is a linear coupling code based on a multipole theory of waveguide arrays and an experimentally validated linear coupling theory. The coupling between the two codes was done through the charge density used to model the grill. This model was then used in Publications II–IV.

The surface charge density corresponding to the discontinuity of the radial electric field at the grill mouth is

$$\sigma(x_0, z) = \epsilon_0 \left[E_x^{\mathrm{pl}}(x_0, z) - E_x^{\mathrm{wg}}(x_0, z)\right]. \tag{3.9}$$

Here, the superscripts denote the plasma and waveguide side with respect to the grill mouth located at x_0. The radial field component in the waveguide, E_x^{wg}, is obtained directly from the SWAN output. From SWAN, we also obtain the toroidal field inside the waveguides, $E_z^{\mathrm{wg}}(x_0, z)$. Since the toroidal component is continuous over the surface, this gives directly the toroidal field on the plasma side. However, to obtain the radial field component on the plasma side in terms of the toroidal field component, the Maxwell equations are used. In the electrostatic approximation, the Fourier-transformed radial field component on the plasma side reads

$$E_x^{\mathrm{pl}}\left(x_0, n_\parallel\right) = \frac{n_\parallel}{S} y_s(n_\parallel) E_z^{\mathrm{pl}}(x_0, n_\parallel), \tag{3.10}$$

where the plasma surface admittance y_s and E_z^{pl} are obtained from SWAN.

After the inverse Fourier transform, the surface charge density is obtained. The absolute value of the surface charge, σ_0, is used as the amplitude and the phase of σ_0 as the phase, $\varphi(z)$, in the oscillating charge density used to model the grill

$$\rho(x_0, z) = |\sigma_0(x_0, z)| \cos\left(\omega t + \varphi(z)\right) \delta(x - x_0). \tag{3.11}$$

More details on the grill model are given in Publication III and Reference [37]. The technical realisation and details are presented in Reference [78].

Figure 3.5 shows the charge density obtained from the coupling to the SWAN code. Compared to the previous model the charge density looks rather different. In this new model the charge is very peaked to the walls between the waveguides as it was

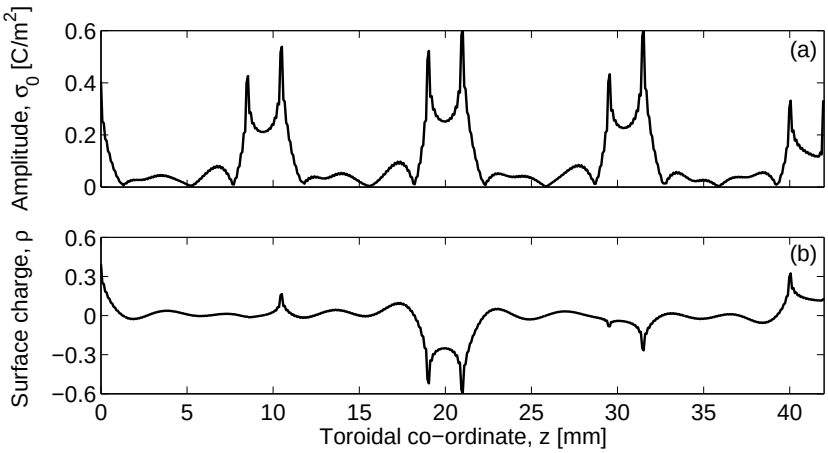

Figure 3.5: The charge density used in the refined model for the reference case. (a) the amplitude σ_0 and (b) the total surface charge density used as the grill.

in the high-$n_\parallel$ case of the phenomenological grill. However, within the waveguides the amplitude is an obscure function which tends to oscillate close to $\rho = 0$.

Due to the electrostatic approximation the low-$n_\parallel$ modes are not preserved correctly in the coupling between SWAN and the PIC code. Therefore, the coupled power obtained from the PIC simulations is rescaled by using the SWAN results. If it is assumed that the power content in the high-$n_\parallel$ part of the spectrum is preserved in the coupling with SWAN, a proportionality equation can be used to give the rescaled coupled power

$$P_{\mathrm{tot}}|_{\mathrm{PIC}} = P(n_\parallel > 9)\big|_{\mathrm{PIC}} \left.\frac{P_{\mathrm{tot}}}{P(n_\parallel > 9)}\right|_{\mathrm{SWAN}} . \tag{3.12}$$

Here, $P(n_\parallel > 9)\big|_{\mathrm{PIC}} = \sum_{n_\parallel > 9} S(n_\parallel)$ is the power content of the modes with $n_\parallel > 9$, which are assumed to be presented accurately in the PIC code and $S(n_\parallel)$ is obtained from Equation (3.8a). The corresponding quantity obtained from SWAN data is denoted by $P(n_\parallel > 9)\big|_{\mathrm{SWAN}}$ and the total coupled power $P_{\mathrm{tot}}|_{\mathrm{SWAN}}$ is obtained by summing over all the $n_\parallel$ modes in the Poynting flux of SWAN.

3.4 Estimation of Heat Loads on Wall Structures

In this section, an estimate for the heat flux hitting the grill limiter is developed. The power absorbed parasitically by the electrons is deposited on the grill limiters or other wall components that are magnetically connected to the region in front of the launcher. This causes hot spots and possible damage on these components and may lead to impurity influxes.

In the simulations described in this work and in Publications II–IV, four 'typical' waveguides were considered while the launcher of Tore Supra has 32 waveguides. However, the simulations are so short that the electrons do not see the 32 waveguides. The duration also affects the radial deposition profile. Therefore, an estimate for the radial depth of the deposition is needed .

3.4.1 Depth of the Deposition Profile

Initially the velocity distribution is Maxwellian. The parasitic absorption of the LH power modifies the distribution via a process that can be approximated by quasilinear diffusion. The time needed for the modification of the velocity distribution is a few quasilinear diffusion times $\tau_{\mathrm{QL}} = v_{\mathrm{th}}^2/D_{\mathrm{QL}}$, where D_{QL} is the quasilinear diffusion coefficient given in Equation (2.25). Therefore, in order to give correct absorbed power fraction, the simulation should be several diffusion times long i.e. $t_{\mathrm{sim}} \gg \tau_{\mathrm{QL}}$.

Landau damping is proportional to the gradient of the velocity distribution. When a plateau is formed in the distribution in front of the launcher, the absorption becomes very weak. If the radial dimension is not taken into account, this results in saturation of energy absorbed by the electrons. After a certain distance along the grill mouth i.e. after a certain number of waveguides, no more energy can be absorbed [17, 25, 26]. However, the wave penetrates radially deeper inside the plasma where it is absorbed by unperturbed plasma. In this way, the deformation in the velocity distribution extends deeper and deeper inside the plasma. The process stops when the power in the overlapping modes of the spectrum has been absorbed. This determines the radial depth of the power deposition profile in the parasitic absorption.

The process described above is illustrated in Figure 3.6. Consider an ensemble of Maxwellian electrons arriving in front of the launcher from the left, and consider only the particles moving to the right. After a few diffusion times, a plateau is formed in the velocity distribution at the grill mouth. When the plateau at this location is fully formed, the wave is no longer damped in this region but goes through. It is then absorbed further inside the plasma where it encounters Maxwellian plasma. Consequently, the radial depth of the deformed velocity distribution increases when the ensemble of electrons travels to the right. The radial depth of the region of the modified distribution function is denoted by d_{hot} and the distribution is assumed to move to the right with the velocity v_{hot}. The radial depth of the plateau, d_{hot}, is proportional to the distance, $z = v_{\mathrm{hot}}t$, travelled in the toroidal direction (see Figure 3.6):

$$d_{\mathrm{hot}}(z) = d_{\mathrm{abs}}\frac{z}{L_{\mathrm{G}}}. \tag{3.13}$$

After the time $t_{\mathrm{hot}} = L_{\mathrm{G}}/v_{\mathrm{hot}}$, the ensemble of the electrons has passed the grill mouth and the radial depth of the plateau stops increasing. Hence, according to

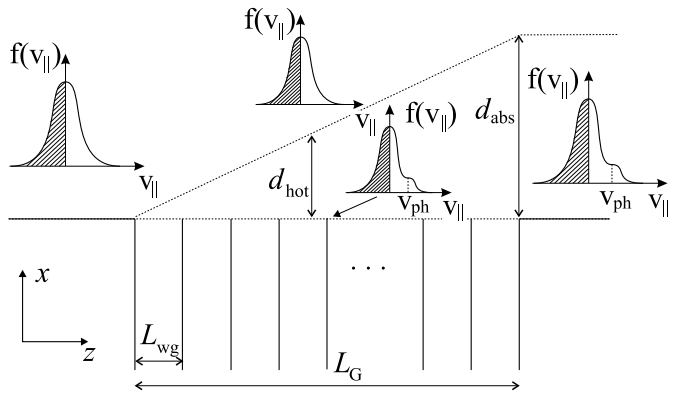

Figure 3.6: Generation of the plateau in the velocity distribution in front of the launcher (Publication III).

the above model the radial depth of the hot electron population leaving the grill region is $d_{\rm abs} = d_{\rm hot}(L_G)$.

We can now use Equation (3.13) to estimate the radial depth of the power deposition profile for the full launcher having 32 waveguides. We find

$$d_{\rm abs} = d_{\rm sim}\frac{L_{\rm G}}{z_{\rm sim}}, \tag{3.14}$$

where $z_{\rm sim}$ is the toroidal distance travelled by the hot electrons in the simulation time $t_{\rm sim}$.

3.4.2 Heat Loads on the Grill Limiters

The geometry used in the following analysis is presented in Figure 3.7. The magnetic field is perpendicular to the waveguides. The area of the hot spot on the wall is roughly $A_{\rm spot} = d_{\rm abs}h_{\rm spot}/\cos\theta$, where $h_{\rm spot}$ is the poloidal extent of the spot. The angle between the magnetic field and the normal of the limiter surface is θ, see Figure 3.7.

The power absorbed in front of the launcher is $P_{\rm abs} = I_{\rm abs}A$, where $A = L_{\rm G}h_{\rm spot}$. The electrons can be accelerated preferentially in one direction. Assume that a fraction η of the absorbed power ends up on the right-hand side limiter. The rest $(1-\eta)$ ends up on the left-hand limiter. Consequently, the heat flux on the right-hand limiter is

$$q''_{\rm hot} = \eta\frac{P_{\rm abs}}{A_{\rm spot}} = \eta I_{\rm abs}\frac{L_{\rm G}}{d_{\rm abs}}\cos\theta = \eta I_{\rm abs}\frac{z_{\rm sim}}{d_{\rm sim}}\cos\theta. \tag{3.15}$$

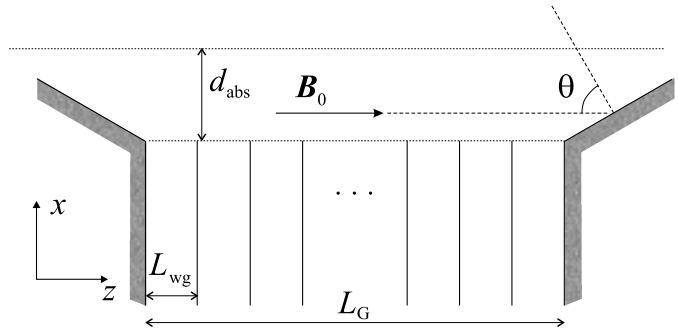

Figure 3.7: The geometry of the heat load calculations (Publication III).

The last equality is obtained with the aid of Equation (3.14). This means that in the simulation with four waveguides the correct heat flux on the grill limiter is obtained. The radial depth of the hot spot is, however, smaller than for the full launcher according to the scaling law in Equation (3.14).

The fraction of power carried to the right-hand limiter, η, is obtained from the velocity distributions. The fraction η is the normalised change in the kinetic energy. The angle $\theta = 75°$ used in the calculations has been deduced from the geometry of the Tore Supra lateral protection limiter.

Chapter 4

Simulation Results on Parasitic Absorption

In this chapter, the simulation results obtained from the PIC calculations on the parasitic absorption are discussed. In parasitic absorption, the short-wavelength modes emitted by the grill are absorbed within a very short distance in front of the LH grill. Typically, about 1% of the LH power was found to be absorbed by electrons within this narrow region giving rise to a population of fast electrons. These energetic electrons are the probable reason for the formation of the hot spots on the limiters [11, 19].

In all the calculations presented in this chapter, the grill model obtained by coupling to SWAN is used. First, the density dependence is discussed followed by a study of the power dependence. Finally, the temperature study is presented. The density dependence was studied in Publication II, and the power and temperature dependencies in Publications III–IV.

4.1 Density Dependence

The density dependence of the power fraction lost on the inclined divertor plates due to parasitic absorption of LH power at the edge was studied experimentally at TdeV [13]. At lower densities, no clear dependence could be seen. However, at higher densities, the loss fraction increased strongly.

Figure 4.1 shows how the power content in the high-$n_\parallel$ modes depends on the density. The lines indicate the fraction of power that is carried by the modes with

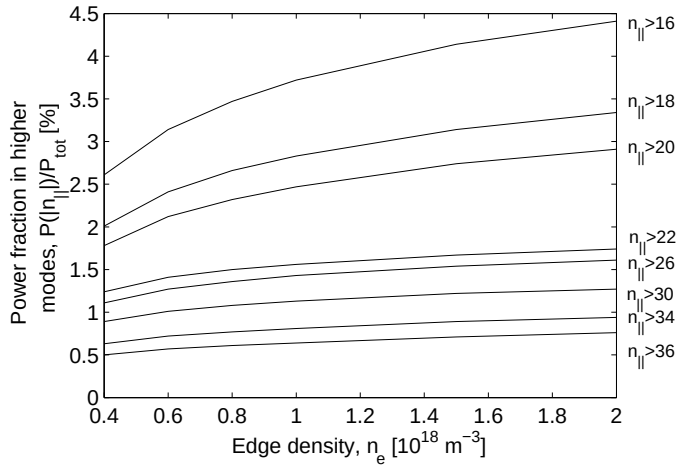

Figure 4.1: The density dependence of the power content in the high-$n_\parallel$ modes with $|n_\parallel|$ larger than the value indicated on the right hand side of the figure. The power fraction is calculated from SWAN.

$|n_\parallel|$ larger than the value indicated on the right-hand side. These results have been obtained from the SWAN calculations. The figure reveals the power fraction that is available for parasitic absorption if we assume that the modes above a threshold $n_\parallel$-value are completely absorbed. As can be seen, the density dependence in this regime is not very strong.

In order to study the density dependence of the parasitic absorption in front of the grill, four different edge densities were used in the PIC calculations. In these simulations, the grill geometry of Tore Supra was used. The plasma and grill parameters are given in Table 4.1.

The density scan was done for an edge temperature of $T_\mathrm{e} = 25$ eV in Publication II and in Reference [79]. The four PIC simulations were performed for typical spectra of Tore Supra with increasing edge densities of $n_{\mathrm{e}0} = 0.6 \times 10^{18}$ m^{-3}, 1×10^{18} m^{-3}, 1.5×10^{18} m^{-3} and 2×10^{18} m^{-3}. The density scale lengths were $L_n = n_{\mathrm{e}0}/n'_\mathrm{e} = 0.6$ cm, 1.0 cm, 1.5 cm and 2.0 cm, respectively. The intention was to find out whether the parasitic absorption depends on the edge density in front of the LH grill. The simulation parameters are summarised in Table 4.1.

In the PIC simulations, the coupled power was calculated with the help of SWAN. The coupled power densities are between 35 MW/m^2 and 48 MW/m^2, see Table 4.1. The absorbed power near the grill mouth was measured with the method described in Section 3.2 and in Publication I. The absorbed power varied from 250 kW/m^2 to 350 kW/m^2 resulting in an absorption of 0.7% to 0.8%, see Table 4.1.

Table 4.1: Simulation parameters for the study of the dependence of parasitic absorption on the edge density for Tore Supra ($T_e = 25$ eV).

Edge density, n_{e0} [10^{18} m^{-3}]	0.6	1.0	1.5	2.0
Maximum density, n_{ea} [10^{18} m^{-3}]	3.0	5.0	7.5	10
Density scale length, n_{e0}/n'_e [cm]	0.6	1.0	1.5	2.0
Magnetic field, B [T]		2.78		
Grill frequency, f [GHz]		3.7		
Width of a waveguide, L_{wg} [mm]		10.5		
Scaled power, I_{in} [MW/m^2]	48	35	35	36
Absorbed power, I_{abs} [kW/m^2]	350	250	280	270
Absorption, I_{abs}/I_{in} [%]	0.73	0.72	0.80	0.76
Electron energies, $E_{e,max}$ [keV]	1.6	1.2	0.6	0.5

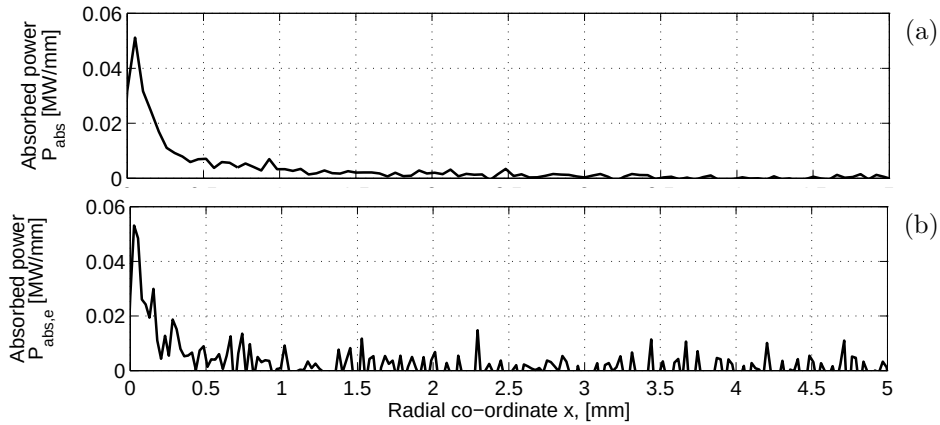

Figure 4.2: Absorbed power density versus radial co-ordinate for the simulation with (a) the lowest density $n_{e0} = 0.6 \times 10^{18}$ m^{-3} and (b) the highest density $n_{e0} = 2 \times 10^{18}$ m^{-3}. Note, that the coupled powers are different in the two cases, see Table 4.1.

Figure 4.2 shows the absorbed power density profiles for the simulation with the lowest and highest edge densities. The absorption is peaked very close to the plasma in front of the grill in both cases. In the low-density case, 350 kW/m^2 is absorbed within 2.4 mm in front of the grill mouth and in the high-density case the absorbed power density is 270 kW/m^2. Note, however, that the coupled powers are different in the two cases.

The absorption can also be seen in the parallel velocity distributions of the electrons. Figure 4.3 shows examples of the distributions at two distances from the grill for the two extreme densities. The frames on the left show the distributions

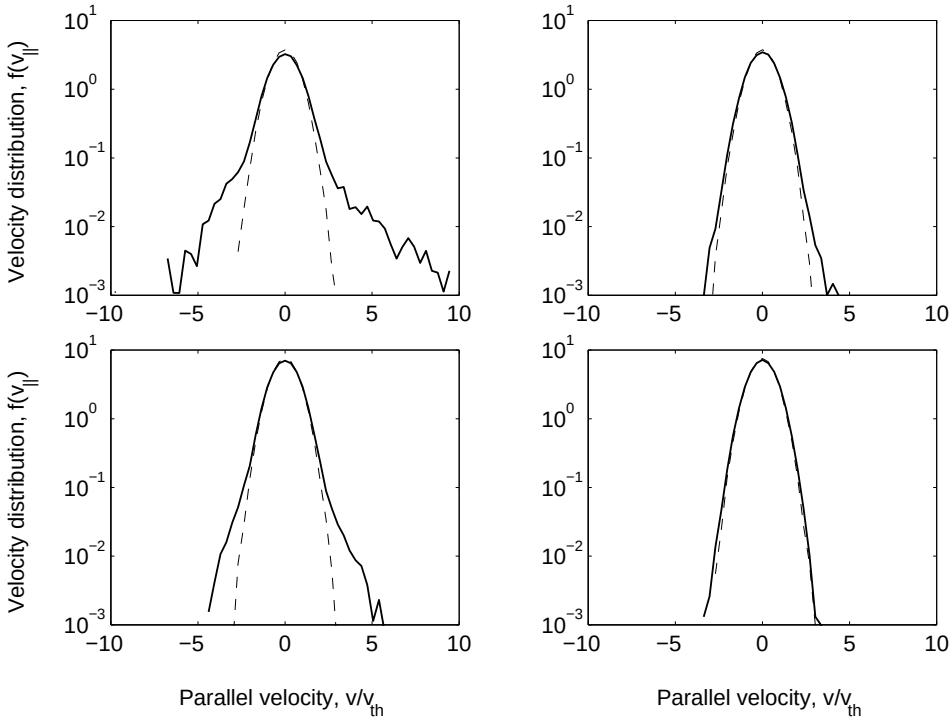

Figure 4.3: The parallel velocity distributions in front of the LH grill in the region $0 < x < 1$ *mm (left) and* $3\ mm < x < 4$ *mm (right): for the simulation with (a) the lowest density* $n_{e0} = 0.6 \times 10^{18}\ m^{-3}$ *and (b) the highest density* $n_{e0} = 2 \times 10^{18}\ m^{-3}$. *Both the initial Maxwellian distributions (dashed line) and the distributions at the end of the simulations (solid lines) are shown [79].*

closest to the grill while the ones on the right-hand side show the distributions at a distance of 3 to 4 mm inside the plasma. The distributions closest to the grill show remarkable broadening. They are, however, broadened in both directions indicating that there are wave modes propagating with both positive and negative phase velocities. Already a few millimetres away from the launcher, the fast electron tail disappears.

In the simulation with the lowest density, a remarkable increase in the hot electron population occurs. Note, however, that in this case the coupled power, as well as the absorbed power, was higher than in the other ones. The parallel velocities extend up to $v_\parallel \simeq 8v_e$. This corresponds to a maximum kinetic energy of 1.6 keV. Further inside the plasma, the electrons remain thermal. In the simulation with the highest edge density, the electrons are accelerated up to velocities $v_\parallel \simeq 5v_e$, corresponding to energies of about 0.5 keV. The maximum energies of the electrons are summarised in Table 4.1.

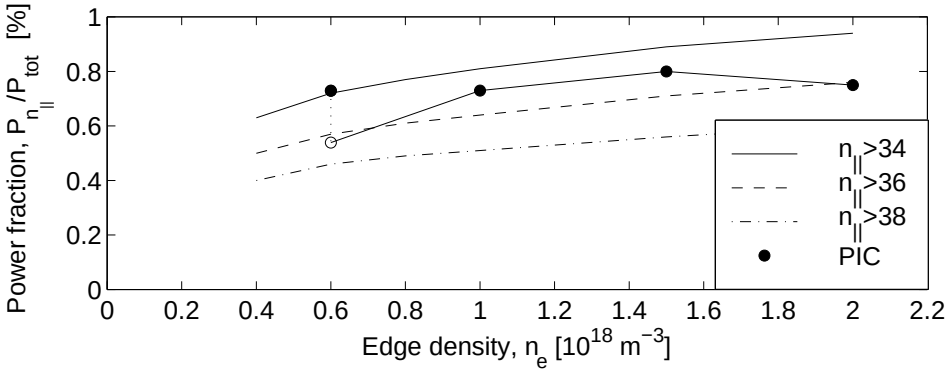

Figure 4.4: Power fraction absorbed in the edge ($0 < x < 2.4$ mm) in front of the LH grill versus the edge density. The bullets denote the simulations results and the lines the power fraction in the high-$n_\parallel$ part of the spectrum of SWAN *as denoted in the figure. The open bullet denotes the simulation point where the power of the simulation with the lowest edge density has been scaled down to the same level as in the other cases [81].*

Figure 4.4 shows the absorption in the PIC simulations compared with the power content of the high-$n_\parallel$ modes obtained from SWAN. A fairly good agreement is obtained with the parasitic absorption and the power content of the modes with $n_\parallel \gtrsim 36$. This means that the parasitic absorption and the generation of the fast electrons can be well explained if all the power in these modes is assumed to be absorbed near the edge. At the temperature used in the simulations, $T_\mathrm{e} = 25$ eV, the mode $n_\parallel = 36$ corresponds to the parallel electron velocity of $v_\parallel \simeq 2.8 v_\mathrm{e}$. The same range of wave modes was also obtained for JET calculations in Publication II and in Reference [80].

In the simulations with a higher temperature of $T_\mathrm{e} = 100$ eV presented in Reference [37], the corresponding comparison of the parasitic absorption with the power content in the SWAN spectra resulted in an agreement with modes $n_\parallel \gtrsim 20$. At this higher temperature, $n_\parallel$=20 corresponds to parallel electron velocity $v_\parallel \simeq 2.5 v_\mathrm{e}$, which is about the same as in the lower temperature case at $T_\mathrm{e} = 25$ eV. However, in the high-temperature case the input power was quite high and varied a lot, which was not taken into account in the comparison. Reducing the power would slightly increase the $n_\parallel$-value.

4.2 Power Dependence

The work done by Mailloux *et al.* [13] showed that the heat fluxes on the limiters increase strongly with the launched LH power. Moreover, the shape of the curves

Table 4.2: Parameters of the plasma and the launcher (Publication III).

Edge density, n_{e0} [m^{-3}]	1×10^{18}
Maximum density, n_{ea} [m^{-3}]	5×10^{18}
Density scale length, n_{e0}/n'_{e0} [cm]	1.0
Magnetic field, B [T]	2.78
Initial electron temperature, T_e [eV]	25
Grill frequency, f [GHz]	3.7
Width of a waveguide, L_{wg} [mm]	8.5
Wall between waveguides, L_{wall} [mm]	2.0
Toroidal width of simulation, L_z [mm]	42
Radial length of simulation, L_x [mm]	97
Number of simulation particles	27 664 597

indicates that this behaviour is strongly non-linear. The strong non-linear dependency on the injected RF power was experimentally confirmed by Goniche *et al.*[17].

Theoretically, it was suggested that the power dependence is due to overlapping of the trapping regions of the wave modes in energy space [19]. With increasing power, and consequently increasing electric field, the overlapping of the modes also increases. Therefore, modes with lower and lower $n_\parallel$-values can participate in stochastic acceleration.

In order to resolve the power dependence of the parasitic absorption, a series of PIC simulations was performed with different coupled power densities. The power dependence of the parasitic absorption is discussed in Publication III.

The grill parameters were chosen to correspond to those of the Tore Supra LH grill. Four 'typical' waveguides, i.e. one module, were used in the simulations. The radial length of the simulation box was chosen to be five perpendicular wavelengths of the principal mode $n_{\parallel 0}$=1.92, where the wavelength was calculated at the low-density edge. The initial temperature was assumed to be $T_e = 25$ eV. The simulation parameters are summarised in Table 4.2.

A set of six simulations was carried out, in which the coupled power density was varied between 26 and 67 MW/m^2. The coupled and absorbed powers were again calculated as described earlier. Figure 4.5 shows the absorption profiles for three different power levels. In each case, the absorption is very peaked at the edge but increases strongly with the coupled power. The peak level in the profiles clearly scales with the power. The absorbed power within 2.4 mm varies from 150 to 710 kW/m^2 and is given in Table 4.3. The parasitically absorbed power fraction, I_{abs}/I_{in}, increases from 0.5 to 1.1% with increasing coupled power.

The absorption can also be seen in the velocity distributions shown in Figure 4.6 for the same three power levels as in Figure 4.5. On the left-hand side are the

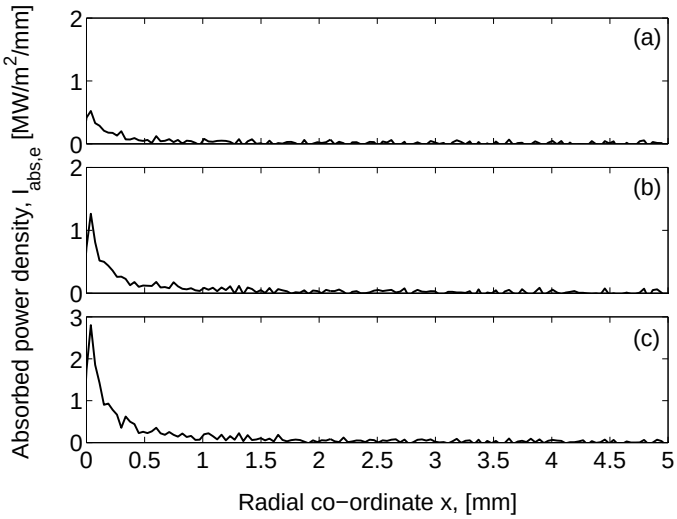

Figure 4.5: Absorbed power density versus radial co-ordinate for (a) low ($I_{\mathrm{in}} = 26\ MW/m^2$), (b) intermediate ($I_{\mathrm{in}} = 41\ MW/m^2$) and (c) high ($I_{\mathrm{in}} = 67\ MW/m^2$) coupled powers ($T_{\mathrm{e}} = 25\ eV$). Note the different scale in frame (c) (Publication III).

distributions just in front of the grill, while the right-hand side shows them further inside the plasma. Closest to the grill, there is a clear broadening in the velocity distributions, which increases strongly with the coupled power. Further inside the plasma, the distribution remains essentially thermal even though a start of modification is seen in the distribution with the highest power density.

From the velocity distributions, the maximum kinetic energies can be determined. In the low-power case, shown in Figure 4.6(a) the fastest particles reach a velocity of about $v_{\parallel} \simeq 5v_{\mathrm{th}}$. This corresponds to a maximum kinetic energy of $E_{\mathrm{e,max}} \approx 0.6$ keV. In the intermediate case of Figure 4.6(b), the maximum velocity is $v_{\parallel} \simeq 7v_{\mathrm{th}}$ resulting in an energy of $E_{\mathrm{e,max}} \approx 1.2$ keV. Figure 4.6(c) shows the high-power case in which the fast electrons reach a velocity of $v_{\parallel} \simeq 9v_{\mathrm{th}}$ or a maximum kinetic energy of $E_{\mathrm{e,max}} \approx 1.8$ keV. The kinetic energies are summarised in Table 4.3.

Table 4.3: Dependence of the parasitic absorption on the coupled LH power ($T_{\mathrm{e}} = 25\ eV$) (Publication III).

Coupled intensity, I_{in} [MW/m^2]	26	35	37	41	50	67
Absorbed intensity, I_{abs} [kW/m^2]	150	250	270	320	420	710
Absorbed power fraction, $I_{\mathrm{abs}}/I_{\mathrm{in}}$ [%]	0.57	0.72	0.74	0.78	0.85	1.1
Maximum electron energy, $E_{\mathrm{e,max}}$ [keV]	0.6	1.2	1.2	1.2	1.6	1.8

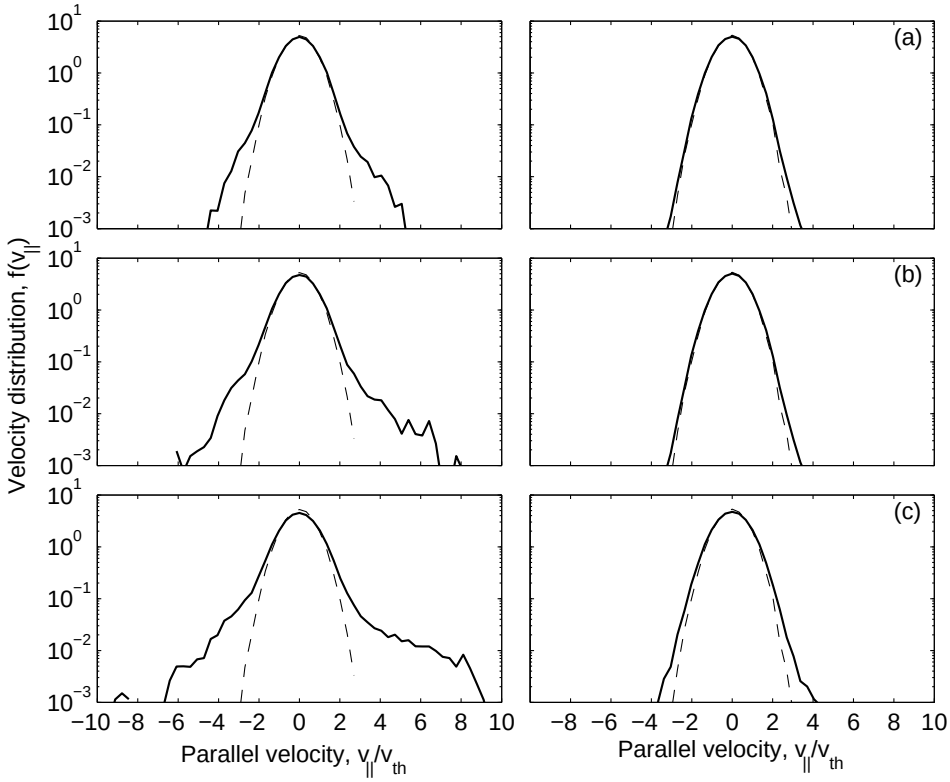

Figure 4.6: Parallel velocity distributions in front of the LH grill in the regions $0 < x < 1$ *mm (left) and* $3 < x < 4$ *mm (right). The distributions are shown for (a) low (*$I_{\mathrm{in}} = 26$ *MW/m*^{2}*), (b) intermediate (*$I_{\mathrm{in}} = 41$ *MW/m*^{2}*) and (c) high (*$I_{\mathrm{in}} = 67$ *MW/m*^{2}*) coupled powers. Both the initial Maxwellian distributions at* $T_{\mathrm{e}} = 25$ *eV (dashed lines) and the distribution at the end of the simulation (solid lines) are shown (Publication III).*

Figure 4.7 recapitulates the parasitic absorption obtained with the PIC simulations. Due to the decreasing signal-to-noise ratio with the wave power, coupled powers lower than $I_{\mathrm{in}} \simeq 25$ MW/m^2 were not studied. Consequently, it was not possible to determine the existence of a possible power threshold from the simulations. However, if one assumes that a threshold exists, one could deduce that its value is below 25 MW/m^2.

The simplest assumption is that the absorbed power increases linearly with the coupled power, i.e. $I_{\mathrm{abs}} = aI_{\mathrm{in}} + b$. In the least-squares fit to the results, the coefficients are $a = 0.0136$ and $b = -0.229$ MW/m^2. The result is shown in Figure 4.7(a). The absorbed power fractions are shown in the lower frame of Figure 4.7(a) and are obtained as $I_{\mathrm{abs}}/I_{\mathrm{in}} = a + b/I_{\mathrm{in}}$. The linear extrapolation gives a threshold power of $I_{\mathrm{thr}} \approx 17$ MW/m^2.

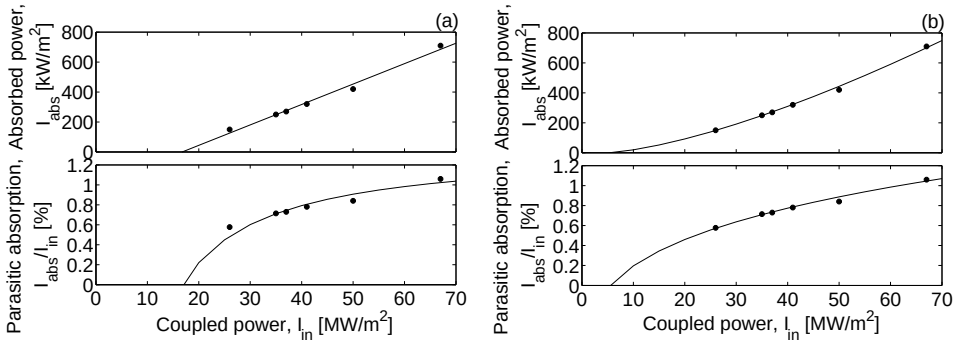

Figure 4.7: Power absorbed in the edge ($0 < x < 2.4$ mm) in front of the LH grill versus the coupled power. The bullets denote the simulations results and the lines in (a) a linear fit and in (b) a non-linear fit (Publication III).

In order to obtain the threshold power density, more analysis is needed. The dependence is not necessarily linear and in fact, experiments suggest a non-linear dependency [13,17]. Also, there are no theories for how the absorbed power or the power fraction should depend on the coupled power. This makes the estimation of the threshold intensity difficult. Therefore, in the following a non-linear fit is made.

While considering the different modes in the LH spectrum, one may notice that the larger is $n_\parallel$ the closer to each other are the modes in velocity space. The lowest $n_\parallel$-value participating in the absorption is determined by the trapping velocity. The trapping velocity for the Fourier mode $E_{k_\parallel}$ is given in Equation (2.24). Consequently, we have $v_{\rm tr} \propto E^{1/2} \propto I_{\rm in}^{1/4}$. We next assume that the edge electrons in front of the grill absorb the power fraction in the modes overlapping each other. Therefore, the parasitically absorbed power fraction is proportional to the trapping width:

$$\frac{I_{\rm abs}}{I_{\rm in}} = a_1 v_{\rm tr} + a_2 = a_1 I_{\rm in}^{1/4} + a_2. \tag{4.1}$$

Here, the coefficients a_1 and a_2 are determined from the simulation results. With the non-linear least-square method we obtain $a_1 = 2.48 \times 10^{-4}$ $({\rm W/m^2})^{-1/4}$ and $a_2 = -0.012$. The curves obtained this way are shown in Figure 4.7(b). This non-linear scaling law gives a threshold power of $I_{\rm thr} \approx 5.5$ MW/m^2.

The discussion above shows that it is not possible to estimate accurately the power threshold from the present PIC simulations. The results show, however, that if a threshold exists it is below 25 MW/m^2. According to the extrapolations discussed above, the most likely value for the threshold is between 5.5 and 17 MW/m^2. Experiments done for the Tore Supra new launcher show a power threshold of 12 MW/m^2 [69], which is within the power density range given by the PIC simulations.

In Publication III, the heat load due to the parasitic absorption is estimated according to the theory presented in Section 3.4. In the following, we consider the simulation with $I_{\mathrm{in}} = 41$ MW/m^2 in more detail. The velocity distributions found in this simulation are shown in Figure 4.6(b). The simulation time was $t_{\mathrm{sim}} = 2.9$ ns and the velocity of the hot electrons was $v_{\mathrm{hot}} \approx 5v_{\mathrm{th}}$. Consequently, the distance travelled by the hot electrons during the simulation is $z_{\mathrm{sim}} = v_{\mathrm{hot}}t_{\mathrm{sim}}$, which yields $z_{\mathrm{sim}} \approx 43$ mm. Figure 4.5 shows that the depth of the radial deposition profile in the reference simulation was $d_{\mathrm{sim}} \approx 0.5$ mm. For Tore Supra, the width of the grill is $L_{\mathrm{G}} = 376$ mm and, therefore, the radial depth of the deposition profile is approximately $d_{\mathrm{abs}} = 4.4$ mm according to Equation (3.14). The depths of the deposition profiles for the full launcher as a function of the coupled power density are presented in Table 4 of Publication III. The depths are found to vary between 3 and 6 mm. The heat loads as a function of the coupled power are also presented in Table 4 of Publication III. The heat load increases from 1.5 to 12 MW/m^2 when the coupled power grows from 26 to 67 MW/m^2.

The parasitic absorption and the heat loads for the newer launcher of Tore Supra [82] are discussed in Publication IV. The absorbed power densities are between 110 and 400 kW/m^2 resulting in an absorption fraction of 0.8 to 1.3%, when the power density increases from 13 to 30 MW/m^2. The estimated power threshold is now 8 MW/m^2. The heat loads range from 1 to 7 MW/m^2 and depend on the coupled power density.

4.3 Temperature Dependence

In order to resolve the temperature dependence of the parasitic absorption, a set of four simulations at different temperatures was performed. The plasma parameters were those given in Table 4.2. The simulations with $T_{\mathrm{e}} = 25$ eV and $I_{\mathrm{in}} = 41$ MW/m^2 was chosen as a reference case. The power density is slightly higher than is usual in experiments, but will serve for the purposes of this work. This power level allows a good enough signal-to-noise ratio and is not too far from the realistic values.

In addition to the reference temperature, one lower $T_{\mathrm{e}} = 12.5$ eV and two higher temperatures $T_{\mathrm{e}} = 50$ eV and 100 eV were chosen. This time the coupled power was kept approximately constant. The parameters can be seen in Table 4.4.

Figure 4.8 shows the absorption profiles for the two extreme temperatures. In the low-temperature case, shown in Figure 4.8(a), the peak value of the absorption profile is clearly lower than in the reference case, in Figure 4.5(b). On the other hand, in the high-temperature case with $T_{\mathrm{e}} = 100$ eV, shown in Figure 4.8(b), the peak power is much larger than in the reference case. The two cases with the extreme temperatures are to some extent comparable to the two extreme power density cases shown in Figures 4.5(a) and (b).

Table 4.4: Dependence of the parasitic absorption on the edge temperature (Publication III).

Initial electron temperature, T_e [eV]	12.5	25	50	100
Coupled intensity, I_{in} [MW/m^2]	41	41	40	40
Absorbed intensity, I_{abs} [kW/m^2]	170	320	470	670
Absorbed power fraction, I_{abs}/I_{in} [%]	0.41	0.78	1.2	1.7
Maximum electron energies, $E_{e,max}$ [keV]	1.0	1.2	1.3	1.6

In the low-temperature case the absorbed intensity within 2.4 mm is 170 kW/m^2 resulting in an absorption of 0.41% of the coupled power. The absorbed power density in the high-temperature case is 670 kW/m^2 and the absorbed power fraction is 1.6%. The absorbed power densities and power fractions are summarised in Table 4.4.

Figure 4.9(a) shows the parallel velocity distribution in the low-temperature simulation while the high-temperature simulation is shown in Figure 4.9(b). The broadening close to the grill is also seen in these two cases though it is not as strong for the high-temperature case as for the low-temperature case. Note, however, that the parallel velocity is normalised to the thermal velocity of the corresponding temperature. Therefore, the widths of the initial distributions look the same in the low and the high-temperature simulations even though in unnormalised velocity space the distribution of the high-temperature case is much wider.

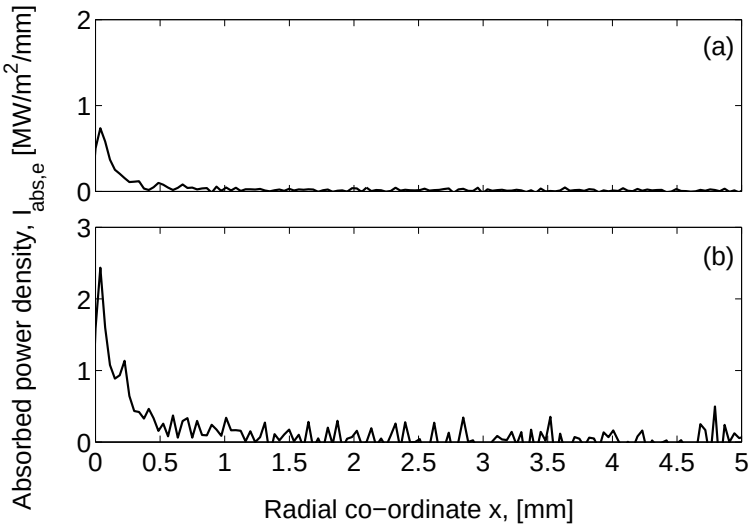

Figure 4.8: Absorbed power density versus radial co-ordinate for (a) low (T_e = 12.5 eV) and (b) high ($T_e = 100$ eV) initial edge temperature ($I_{in} \approx 41$ MW/m^2). Note the different scaling (Publication III).

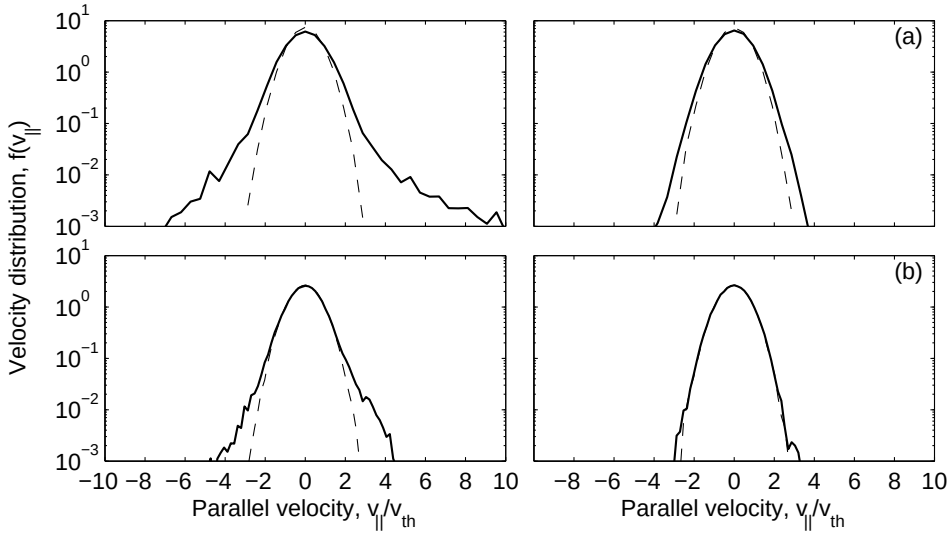

Figure 4.9: Parallel velocity distributions in front of the LH grill in the regions $0 < x < 1$ *mm (left) and* $3 < x < 4$ *mm (right) for (a) low* ($T_\mathrm{e} = 12.5$ *eV) and (b) high* ($T_\mathrm{e} = 100$ *eV) initial temperature* ($I_\mathrm{in} \approx 41$ *MW/m*^{2}*). Both the initial Maxwellian distributions (dashed lines) and the distribution at the end of the simulation (solid lines) are shown. Note, that even though the initial distributions look the same in both cases (a) and (b), the distribution in the high-temperature case is much wider. This is due to the normalisation to the thermal velocity of the corresponding temperature.*

The velocity of the fastest electron population in the low-temperature case is $v_\parallel \simeq 9v_\mathrm{th}$ corresponding to a maximum energy of $E_\mathrm{e,max} \approx 1.0$ keV. In the high-temperature case, the fastest electrons have the velocity $v_\parallel \simeq 4v_\mathrm{th}$. This corresponds to a maximum energy of $E_\mathrm{e,max} \approx 1.6$ keV. The maximum energy of the low-temperature case corresponds to the phase velocity of the mode $n_\parallel \approx 16$ while in the high-temperature case the corresponding mode is $n_\parallel \approx 13$. Note that, consequently, the fastest electrons in Figures 4.9(a) and (b) are interacting roughly with the same part of the LH spectrum. The results of the temperature scan are summarised in Table 4.4.

In the following, the wave spectrum is assumed not to change with the temperature. However, when the temperature increases, the velocity distribution gets broader and, therefore, the thermal velocity approaches higher phase velocities. Consequently, modes with lower $n_\parallel$ are involved in the absorption, and more electrons reach the region where the overlapping of the modes and the absorption starts. In fact this can be seen in the power spectra of the simulations with different temperatures.

In the low-temperature case ($T_\mathrm{e} = 12.5$ eV), we find a good agreement if we assume that all the power in the modes with $n_\parallel > 41$ is absorbed. The phase velocity of this

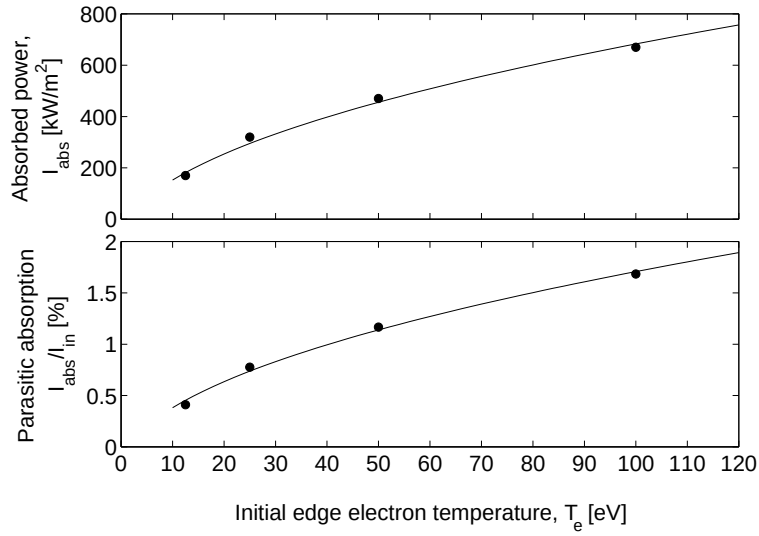

Figure 4.10: Power absorbed in the edge ($0 < x < 2.4$ mm) in front of the LH grill versus the edge temperature. The bullets denote the simulations results (Publication III).

mode is $v_{\mathrm{ph}} \approx 3.5 v_{\mathrm{th}}$. In the high-temperature case ($T_{\mathrm{e}} = 100$ eV), the absorption is in agreement with the power content in the modes with $n_{\parallel} > 22$, which corresponds to a phase velocity of $v_{\mathrm{ph}} \approx 2.3 v_{\mathrm{th}}$.

The width of the velocity distribution is proportional to the thermal velocity and, consequently, to the square root of the temperature: $I_{\mathrm{abs}}/I_{\mathrm{in}} = b_1 T^{1/2} + b_2$. According to the least-squares fit to the simulation results, the coefficients are $b_1 = 1.94 \times 10^{-3}$ eV$^{-1/2}$ and $b_2 = -2.32 \times 10^{-3}$. This simple model seems to agree quite well with the simulation data shown in Figure 4.10. Temperatures lower than 12.5 eV have not been investigated because the absorption is so low in that range. Moreover, it is not meaningful to study the very low temperature range since the edge temperature of 5–10 eV seems to be an operational limit causing disruptions in Tore Supra [83].

In Publication III, the heat load and the deposition depth were also calculated as a function of temperature for the old launcher. The values of both the absorption depths and the heat loads were in the same range as for the power scan: the deposition depth was roughly from 3 to 6 mm and the heat loads from 2 to 12 MW/m^2.

For the new launcher the heat loads were studied in Publication IV. The load again increased with the temperature, being 1 MW/m^2 for the lowest temperature and about 5 MW/m^2 for the highest. However, the increase was not as strong as for the former launcher.

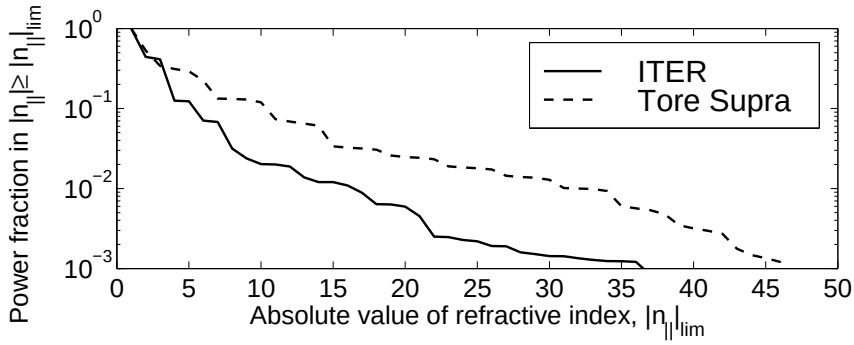

Figure 4.11: Power content in the higher $n_{\parallel}$ modes for the LH launchers of ITER and Tore Supra.

4.4 Absorption in front of the ITER Grill

The parasitic absorption of the LH power in the edge plasma in front of the ITER lower hybrid launcher was also investigated [71, 84, 85]. Altogether six simulations were performed. The density in front of the antenna was $n_e = 6.2 \times 10^{18}$ m^{-3}. A linear density profile was used with a density scale length of 1 cm. The magnetic field along the z axis was $B = 4$ T and the frequency of the grill was $f = 5$ GHz. The initial electron temperature ranged from 25 to 100 eV and the coupled power density varied from 14 to 55 MW/m^2. The width of an active waveguide was 9.25 mm and that of a passive waveguide was 7.25 mm. The width of the wall between the waveguides was 3 mm. The phase difference between the active waveguides was $3\pi/2$ and the feeding phase between the eight waveguides' multijunction was zero.

Because of the geometry and the PAM structure of the grill, eight waveguides, i.e. one module, from the middle part of the grill were chosen for the charge density modelling the LH grill. As in the previous cases, the surface charge was obtained from the SWAN calculations.

The design of the ITER LH grill has significantly reduced the power content in the high-$n_{\parallel}$ modes. This can be seen in Figure 4.11 which shows the power content in the modes with $|n_{\parallel}|$ larger than the value shown on the abscissa. We have compared the spectra for ITER and for the Tore Supra new launcher C3 used in Publication IV. There is a clear difference between the power contents in the higher modes in these two launchers, the difference being in favour of ITER. One should note that the densities in front of the launchers are different. For ITER the density is $n_e = 6.2 \times 10^{18}$ m^{-3} but for Tore Supra only $n_e = 10^{18}$ m^{-3}. Apparently, these densities are chosen due to coupling properties, which seem to be affected by the density. The coupling has a clear optimum density [39, 86]. Moreover, the density dependence of the power fraction in the high-$n_{\parallel}$ modes should not be that

pronounced and the power fraction in the highest modes should increase with the density. At least this was the case for the Tore Supra C2 launcher, see Figure 4.1.

The power content in the high-$n_{\|}$ modes is apparently so low that no absorption was observed. For all the cases with various coupled power densities between 14 and 55 MW/m^2, and the different temperatures between 25 and 100 eV, the absorbed power density was negligible. In the velocity distributions no changes were seen.

One should, however, notice that the simulations were very short even though they were computationally demanding. The simulation time of slightly over 3 ns was just a few quasilinear diffusion times.

Chapter 5

Wave Coupling to the Plasma

In the work discussed in the previous sections, the charge density was modelling the grill. In the electrostatic cases no walls were modelled and the waveguides structure as well as the wave propagation inside the waveguides was omitted. The only way the walls and the waveguides were taken into account was in the SWAN calculations. With the electromagnetic particle-in-cell code XOOPIC [74], it is for the first time possible to model the whole grill structure facing the plasma. The EM model also allows taking into account the wave propagation and reflection inside the waveguides.

The electromagnetic PIC simulations on LH coupling are discussed in Publication V. Preliminary results have been published in References [86–88]. In this chapter, the electromagnetic grill model used in Publication V is first described. Then, some diagnostics are presented. The method for obtaining the power spectrum from the PIC calculations is explained together with the reflection coefficient.

5.1 Electromagnetic Model for the Grill

A real rectangular waveguide is fed by the TE_{10} mode, which is the lowest order mode the structure supports. However, XOOPIC is a 2d3v PIC code having two spatial dimensions and three velocity components. Therefore, a 2d-projection is needed. When the poloidal y direction is neglected and the poloidal height of the waveguide is extended to infinity, the TE_{10} mode reduces to the TEM mode. The TEM mode is the principal mode in a parallel plate waveguide, which does not

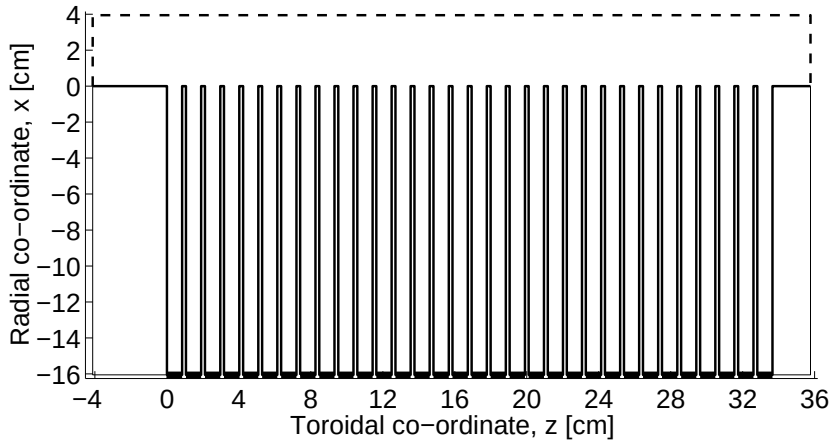

Figure 5.1: The simulation geometry in the electromagnetic case with all the 32 waveguides. The different line types denote different boundaries: the dashed line is an Exitport, which is transparent for the wave, the solid lines are Conductors that model the waveguides and the thick lines at $x \approx -16$ cm are boundaries emitting TEM waves.

support the TE modes. The waveguides are, therefore, modelled as 32 parallel plate waveguides having perfectly conducting walls. The waves are launched one vacuum wavelength away from the grill mouth.

The grill structure is illustrated in Figure 5.1, which shows the geometry used in the electromagnetic simulations. The waveguides can be seen in the lower part of the figure. In the toroidal direction, the boundaries were chosen to be periodic for the particles. For the wave, all the boundaries are non-periodic. At the toroidal ends as well as on the high-density side in the radial direction, so-called ExitPorts are used. The boundary conditions for the waves are such that there is a perfect-match impedance for which in this case the vacuum conditions are used. This means that the boundary is transparent to the wave mode having the impedance of the wall. For other modes, the boundary is semi-transparent. The ExitPort boundaries are denoted with the dashed line in Figure 5.1. The thick line at the lowest part of the figure denotes the boundaries that launch the TEM wave and the solid lines are the conductors that model the waveguide walls.

5.2 Wave Diagnostics

In SWAN, the spectra are calculated from a complex field and, therefore the asymmetric spectrum is easily achieved because the complex field inherently contains the information of the direction of the wave mode. However, in the PIC calculations

we are dealing with real fields. The information of the directions of the wave modes is there, but if we take a field at a given time and at a given radial location, and make the Fourier transform, by the definition of the FFT (Fast Fourier Transform) the signal is symmetric. This can be understood if one thinks of a snapshot of a one-dimensional sinusoidal wave at a given time. Since the wave is stationary and does not have a second dimension, there is no way of telling whether it is travelling to the left or to the right. However, if the wave position or form is known at a later time, the direction of propagation can be determined. The direction can also be defined if the position is known in a second dimension. Consequently, the spectra will always be symmetric if they are calculated from a snapshot of a field at one radial location.

The power spectrum of the wave is, therefore, calculated from the toroidal electric field as a Fourier transform in space and time

$$P\left(x, n_{\parallel}\omega\right) = \mathcal{N} y_s \left| \frac{1}{N_t} \sum_{j=1}^{N_t} \exp\left(\mathrm{i}\omega t_j\right) \widehat{E}_z\left(x, n_{\parallel}, t_j\right) \right|^2 , \tag{5.1}$$

where $\mathcal{N}$ is a normalisation coefficient, y_s is the surface impedance and $\omega = 2\pi f$ is the angular frequency of the wave. The number of time steps used in the time integration of the spectrum is N_t and t_j is the corresponding time. The spatial Fourier transform of the toroidal electric field, E_z, in the z direction is defined as

$$\widehat{E}_z\left(x, n_{\parallel}, t_j\right) = \sum_{k=0}^{N_z-1} E_z(x, z_k, t_j) \, \exp\left(-\mathrm{i} z_k n_{\parallel}\omega/c\right), \tag{5.2}$$

where z_k is the discretised toroidal co-ordinate.

The spectra are normalised to the maximum value of the spectrum at $x = -1$ cm. The vacuum admittance is constant, while the plasma surface admittance is proportional to $\left|1/n_{\parallel}\right|$. This has to be taken into account when normalising the spectra on the plasma side. If the normalisation coefficient in the vacuum is denoted by $\mathcal{N}_{\mathrm{vac}}$, then on the plasma side it is $\mathcal{N}_{\mathrm{vac}} n_{\parallel 0}$, where $n_{\parallel 0}$ is the refractive index of the principal mode.

At the grill mouth, part of the LH power is reflected back into the waveguides. The reflection coefficients of the waveguides are determined from the time-averaged Poynting fluxes, where a decrement is caused by the reflected wave. The coefficient at a given time t is determined from

$$R(t) = \frac{I_{\mathrm{in}} - \mathcal{P}(t)}{I_{\mathrm{in}}}, \tag{5.3}$$

where $\mathcal{P}(t)$ is the time-averaged Poynting flux at the time t and I_{in} is the launched power density. The time averaging is done over a few wave periods.

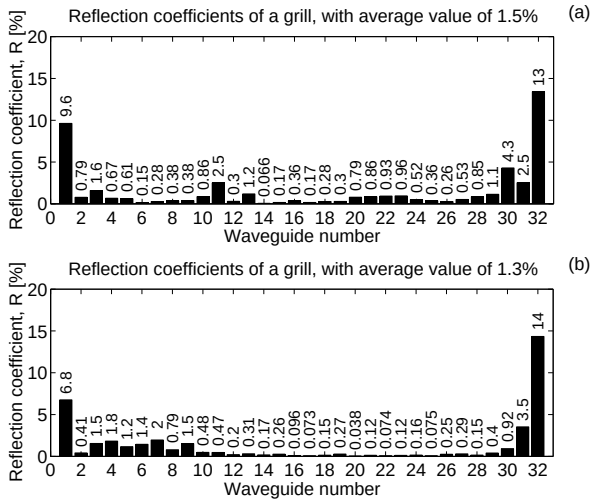

Figure 5.2: Reflection coefficients at the time $t = 3$ ns of a launcher with 32 waveguides. The case with linear density profile is shown in frame (a) and the one with a homogeneous density is shown in (b). The average values are $R_{\mathrm{lin}} = 1.5\%$ and $R_{\mathrm{hom}} = 1.3\%$, respectively.

5.3 Simulation Results

In order to study the coupling of the wave from the waveguides to the plasma, two simulations were carried out in Publication V. For both simulations the Tore Supra grill parameters were adopted. The edge density was $n_{\mathrm{e0}} = 10^{18}$ m^{-3} for both cases but the density profile was changed. In the first case, a homogeneous density was used while in the other case the density profile was linear with a density scale length of $L_n = 1$ cm.

In this first study using an electromagnetic code, we wanted to use as few grid cells as possible. The limiting factor for the cell size is the heating of the electrons due to a so-called non-physical cold beam instability [30]. This instability is purely numerical and occurs due to alias wave modes. The instability tends to heat the plasma until a higher temperature equilibrium is achieved, where the heating due to the instability is equal to the energy losses from transport and field mechanisms. The growth rate of the instability is negligible roughly when $\lambda_{\mathrm{D}}/\Delta z \gtrsim 0.3$ [30], where $\lambda_{\mathrm{De}} = v_{\mathrm{the}}/\omega_{\mathrm{pe}}$ is the Debye length and Δz the toroidal grid spacing. Therefore, a temperature of $T_{\mathrm{e,i}} = 1$ keV was chosen for both electrons and ions. The simulations parameters are summarised in Table 1 in Publication V.

The reflection coefficient of each waveguide is shown in Figure 5.2 for the two simulations. Qualitatively the results look quite similar. There are larger reflection

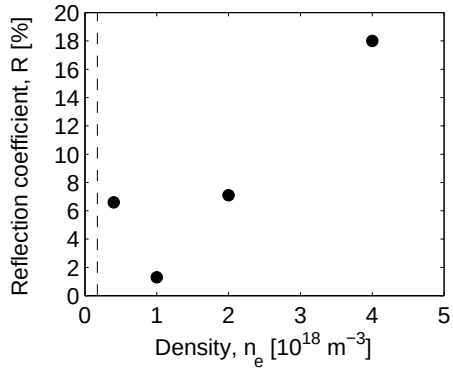

Figure 5.3: Average reflection coefficients versus density.

coefficients at both ends of the grill and very small ones in the centre. However, the reflection varies quite a lot from waveguide to waveguide in each case. At time $t = 3$ ns, the average reflection coefficients are approximately $R_{\mathrm{lin}} = 1.5\%$ for the case with linear density profile and $R_{\mathrm{hom}} = 1.3\%$ for the homogeneous one.

The linear density profile results in a slightly larger reflection than the homogeneous one. However, the results show that for scale lengths larger than or equal to $L_n = 1$ cm the density gradient does not play an important role in the coupling problem. This is in qualitative agreement with SWAN results for JET [89].

Another study with the grill parameters chosen for JET [90] showed that the important parameter is actually the edge density. In this work four simulations with densities of $n_{\mathrm{e0}} = 0.4,\ 1,\ 2$ and 4×10^{18} m^{-3} with homogeneous profiles were performed. The reflection coefficients were calculated in each waveguide. The density dependence of the average reflection coefficients is shown in Figure 5.3. The reflection varied between slightly over 1% and 18%. The dashed line denotes the cut-off density. There is a clear optimum with best coupling close to a density of $n_{\mathrm{e0}} = 10^{18}$ m^{-3}. At this density, the reflection is smallest and, consequently, the coupling is best, while the reflection coefficients grows for both increasing and decreasing densities.

Figure 5.4 shows the power spectrum of the wave versus parallel refractive index for the case with a linear density profile. The grill launches a spectrum containing the principal mode $n_{\|} \approx -1.9$ and its odd harmonics $n_{\|} \approx 5.8, -9.6$ and 13.4. These modes are those of the TEM wave and can be found by an analytic calculation. The agreement with the analytic calculation is fairly good. Figure 5.4(d) shows the spectrum inside the waveguides and (c) just at the mouth.

As can be seen in Figures 5.4(a) and (b), the highest harmonics have been absorbed already within a distance of 1 cm on the plasma side. The first backward propagating harmonic at $n_{\|}$=5.8 is also partly absorbed within the few first cen-

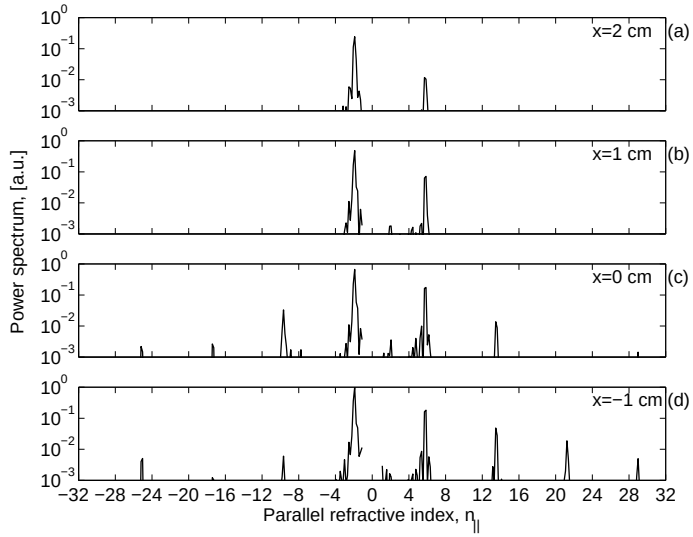

Figure 5.4: Power spectra for the linear density profile versus the parallel refractive index integrated over three wave periods at different distances from the grill mouth: (a) At $x = 2$ cm, (b) at $x = 1$ cm, and (c) at the grill mouth ($x = 0$). Frame (d) shows the spectrum inside the waveguide at $x = -1$ cm (Publication V).

timetres. A clear reduction in this peak can be seen while moving inwards to the plasma centre. The linear Landau damping rate obtained from Equation (2.22) is $L_\gamma(n_\parallel = 5.8) = 4.5$ cm calculated at the density $n_\mathrm{e} = 10^{18}$ m^{-3} and the temperature $T_\mathrm{e} = 1$ keV. At the density $n_\mathrm{e} = 3 \times 10^{18}$ m^{-3} the damping rate is reduced to $L_\gamma = 2.8$ cm. The phase velocity of the mode $n_\parallel = 5.8$ is $v_\mathrm{ph} = 3.9 v_\mathrm{the}$. However, the phase velocity of the principal mode at $n_\parallel = -1.9$, $v_\mathrm{ph} = -11.9 v_\mathrm{the}$, is so high that the mode cannot interact with such plasma. Consequently, no absorption of the principal mode is seen in the wave spectrum. This mode would interact deeper inside the plasma where the temperature is higher.

The lengths of the simulations presented in Publication V were too short in order to see the effect in the tail of the velocity distribution where only few particles are present. The absorption of the mode close to $n_\parallel$=5.8 is barely seen in the velocity distributions close to the grill mouth where the acceleration of electrons has just started. A small deformation of the velocity is also seen at a velocity somewhat above $-2v_\mathrm{the}$, where the mode at $n_\parallel = -9.6$ is absorbed. However, in simulations with a higher power level presented in Reference [86], a clear plateau was found to form around the phase velocity of the mode $n_\parallel$=5.8. In that case, the quasilinear diffusion times were much shorter and the effect in the velocity distribution was much more pronounced. Moreover, the trapping widths were much larger enabling stochastic acceleration over a wider range in the velocity space.

Chapter 6

Summary and Discussion

This thesis reports on the development of the grill model used in particle-in-cell (PIC) codes and their use for simulations of the near-field of the lower hybrid grill. The objective of the thesis is two-fold.

First, the thesis introduces a new tool for the study of the near-field of the LH grill – the PIC method. Usually the wave–plasma coupling is studied with linear coupling codes based on the linear wave equations [31, 32]. The acceleration of the particles in front of the launcher is generally studied with test particle simulations. In this thesis, the coupling problem is investigated with electromagnetic PIC simulations and the acceleration of electrons through parasitic absorption of the LH power with an electrostatic code.

The second aspect of the thesis is to explore the physics behind the hot spots observed on components that are magnetically connected to the grill region. Several experiments have shown hot spot formation and impurity influxes related to the heat loads [10–14]. Experiments on TdeV [13] showed some evidence of the hot spots on the grill limiter being due to fast electrons generated in the scrape-off layer just in front of the grill. So far, no experimental evidence has been found for ions causing the heat loads, although this possibility has not been ruled out either.

The electrostatic PIC code needed a model for the grill, used for launching the wave into the plasma. A large part of the work was spent on this issue. The work started with the simple model used in Publication I. This model was used to present the PIC method as a tool for studying the electron acceleration via parasitic absorption of the high-$n_\parallel$ part of the wave spectrum. In addition, some numerical diagnostics had to be developed for extracting the launched energy and the absorption by the electrons from the simulations. The first simulations proved the feasibility of the code. Even with the simple model a clear difference was seen between the two

cases – one with only a small amount and another one with a fairly large amount of power in the high-$n_\parallel$ modes. A rapid generation of fast electrons was observed in the case with a lot of power in the short wavelength modes while clearly less power was absorbed in the other case. However, it was clear that the grill model needed further refinements in order to better resolve the connection between hot spot formation and the LH-produced fast electrons.

In order to model experiments with a realistic LH spectrum, the PIC code was coupled with the SWAN code. The oscillating charge density used as the grill model in the PIC code was obtained from the output of SWAN. This calculation has been described in Publications II and III as well as in References [37,78–80]. Since the low-$n_\parallel$ part of the spectrum is not very well represented in the electrostatic approximation, the SWAN data was used to take care of this part in the calculation of the coupled power. The electromagnetic SWAN code and the electrostatic PIC code nicely complement each other because the low-$n_\parallel$ part of the spectrum does not interact with the cold edge plasma and is well described by the linear SWAN code. On the other hand, the high-$n_\parallel$ part is well characterised by the electrostatic PIC code, which also takes into account the kinetic and non-linear effects.

The refined grill model with the SWAN spectrum was used to investigate the parasitic absorption in more detail. Experimental observations made at TdeV [13] and Tore Supra [12, 17] have suggested that the power lost through the parasitic absorption increases with the edge density in front of the grill. The density dependence was studied with edge densities ranging from $n_\mathrm{e} = 0.6 \times 10^{18}$ m^{-3} to $n_\mathrm{e} = 2 \times 10^{18}$ m^{-3}. The parasitic absorption seemed to increase with the edge density, though the dependence was not very strong in this range. The absorption followed quite well the power contents in the high-$n_\parallel$ part of the spectrum, when the PIC results were compared with the SWAN spectra for both Tore Supra and JET. At an edge temperature of $T_\mathrm{e} = 100$ eV, the absorption follows approximately the power content in modes $|n_\parallel| \gtrsim 20$ [37], whereas at the lower edge temperature of $T_\mathrm{e} = 25$ eV the modes $|n_\parallel| \gtrsim 35$ (Publication II) are in charge of the parasitic acceleration. At the higher temperature the absorption was about 2% and at the lower one less than 1%.

The experiments also indicate that the parasitic absorption depends on the coupled power [13, 17]. Another study implies that the heat fluxes observed on the grill limiters are actually proportional to the power density [91]. Therefore, a PIC study on the power density dependence was made. The power density was varied from 26 to 67 MW/m^2 with other initial parameters kept constant. The parasitically absorbed power density increased clearly with the coupled power density. The absorption, defined as the ratio of the parasitically absorbed power density to the coupled one, was around 1%. Whether a power threshold exists could not be resolved in this work. However, if it is believed that such a threshold exists, the results indicate that it should be below $I_\mathrm{thr} = 25$ MW/m^2 for the C2 grill of Tore Supra. In order to extrapolate the power dependence to lower power densities, a linear and a non-linear scaling was deduced for the absorption. The non-linear

dependence was derived from a linear dependence on the trapping velocity. It was assumed that the power fraction in the overlapping modes was absorbed by the electrons in front of the grill. The parasitically absorbed power fraction would then be proportional to the trapping width. The extrapolation suggested that the threshold would most likely be between $I_{\mathrm{thr}}^{\mathrm{lin}} = 17$ MW/m^2 and $I_{\mathrm{thr}}^{\mathrm{nl}} = 5.5$ MW/m^2.

The temperature dependence of the parasitic absorption was evident in References [37, 79, 80] and Publication II. However, a systematic study was only done in Publication III. The wave spectrum was assumed not to change with the temperature. The increasing temperature affected clearly the absorption because the velocity distribution became wider. Consequently, more electrons could reach the region in velocity space where the overlapping of the modes started. Subsequently, also the absorption increased. A temperature scaling was also derived based on the proportionality of the absorbed power fraction to the thermal velocity.

The heat loads on the grill limiter due to the parasitic absorption of the LH power was estimated. It was assumed that only the electrons contribute to the effect; the ions were neglected in the whole calculation. It was also assumed that all the power absorbed parasitically by the edge electrons ends up on the walls on either side of the grill. The fraction of power deposited on one side was deduced from the normalised change in the kinetic energy calculated from the velocity distributions. An estimate for the radial deposition depth was needed. A scaling equation was derived for this purpose, because the electrostatic simulations only had four waveguides while the real ones at Tore Supra and JET have 32. The results presented in Publication III were in quite good agreement with the experimental observations [16, 17, 91], both for the heat loads and the deposition depths.

The electromagnetic PIC code XOOPIC was used to study the wave coupling from the waveguides to the plasma. In this study, the main interest was in the low-$n_{\parallel}$ part of the spectrum because these modes are the ones that carry most of the power. Good coupling is crucial for the use of LH current drive in future devices. The main objective of Publication V was to show that the electromagnetic PIC codes are well enough developed for modelling such a complicated system as the LH grill. In this work, two cases with different density profiles were studied. Only a small difference was observed in coupling to a homogeneous plasma with a density well above the cut-off density compared to one with the same edge density but a linear profile with a density scale length of 1 cm. The spectra clearly showed that the higher modes were absorbed in the edge plasma. The absorption was also seen in the velocity distributions in a simulation with a high power density [86]. The advantage of the PIC method in the coupling calculations is that it can also be used to study the coupling at very low densities or at steep gradients. The usual approximations tend to fail at densities close to or below the cut-off density.

The simulations described in this work have several limitations and one should, therefore, be careful when interpreting the results. In the electrostatic simulations, only four waveguides were used even though the Tore Supra grill has 32 waveguides.

Choosing the particular waveguides given by SWAN results has, of course, some effect on the results. The simulations are rather short so that in the simulation time the particles travel a shorter distance than the width of a real grill. At lower power levels, the length of the simulations is a few quasilinear diffusion times, which is just long enough for the hot tail to form in the velocity distribution.

In the work presented in this thesis only the electron contribution to the heat load and parasitic absorption has been taken into account. The sheath formation, the heat loads due to ions and the emission of secondary electrons or ions have been neglected. However, the power available for heating the walls was obtained from the simulations, as conservation of energy implies that it is this power that causes the hot spots even if part of the energy is converted to ions. The sheath formation and the phenomena occurring within the sheath have been studied in References [21, 23]. The sheath potential reduces slightly the kinetic energy of the electrons before they hit the wall. This is compensated for by the increase of the kinetic energy of the ions. The secondary electron emission may enhance the electron heat flux to the wall [92–94] as it tends to reduce the sheath potential.

Lower hybrid waves provide by far the most promising method for efficient off-axis current drive, needed to sustain internal transport barriers. In the 'advanced tokamak scenarios', LH current drive is used to modify the current profile. Good coupling of LH power is, therefore, very important for these scenarios in ITER. The hot spots are detrimental for lower hybrid current drive since they lead to a large impurity influx. Consequently, it is not possible to operate the launchers at full power. The impurity accumulation is especially problematic in 'advanced tokamak scenarios' in discharges with internal transport barriers [95]. Consequently, a good understanding of the plasma phenomena in front of the grill is needed.

The tests of the ITER-type PAM grill in Italy in the beginning of the year 2003 will provide a lot of new information on the topics of this thesis.

Bibliography

[1] Nakicenovic, N., Grübel, A. and McDonald, A. (Eds.), *Global Energy Perspectives* (World Energy Council, Cambridge University Press, Cambridge, UK, 1998).

[2] Wesson, J., *Tokamaks*, no. 48 in Oxford Engineering Science Series (Clarendon Press, Oxford, 1997), second edn.

[3] Tamm, I. E. and Sakharov, A. D., "Теория магнитного термоядерного реактора", в М. А. Леонтович (редактор), *Физика плазмы и проблема управляемых термоядерных реакций*, том 1 (Издателъство Академии Наук СССР, Москва, 1958), 1–41, (in Russian), English translation in "Theory of a magnetic thermonuclear reactor", in M. A. Leontovich (Ed.), *Plasma Physics and the Problem of Controlled Thermonuclear Reactions*, vol. 1 (Pergamon Press, London, 1961), pp. 1–47.

[4] Tore Supra Team, "Toward long-pulse, high-performance discharges in Tore Supra: Experimental knowledge and technological developments for heat exhaust", *Fusion Tech.* **29** (1996), pp. 417–448.

[5] Cordier, J. J. and Tore Supra Team, "Experience gained from series manufacturing of actively cooled plasma facing components and their operation an Tore Supra", *Fusion Eng. & Design* To appear in Proceedings of 22nd Symposium on Fusion Technology, 9–11 September 2002, Helsinki, Finland.

[6] Fisch, N. J., "Theory of current drive in plasmas", *Rev. Mod. Phys.* **59** (1987), pp. 175–234.

[7] Cairns, R. A., *Radiofrequency Heating of Plasmas*, The Adam Hilger Series on Plasma Physics (Adam Hilger, Bristol, 1991).

[8] Tala, T., *Transport Barrier and Current Profile Studies on the JET Tokamak*, Ph.D. thesis, Helsinki University of Technology, Espoo, Otaniemi (2002), VTT Publications 467, VTT Processes, Espoo, 71 p. + app. 95p.

[9] Staebler, A. *et al.*, "The role of neutral beam injection geometry in advanced discharge scenarios on ASDEX Upgrade", in *Europhys. Conf. Abstr.*, vol. 26B (2002), pp. O–5.03, (to appear in the Proceedings).

[10] Goniche, M. *et al.*, "Edge losses during lower hybrid current drive experiments with the ergodic divertor in Tore Supra", in E. Joffrin, P. Platz and P. E. Stott (Eds.), *Europhys. Conf. Abstr.*, vol. 18B Part III (Montpellier, 1994), pp. 1042–1045.

[11] Harris, J. H. *et al.*, "Lower-hybrid wave coupling and impurity generation in Tore Supra", in B. E. Keen, P. E. Stott and J. Winters (Eds.), *Europhys. Conf. Abstr.*, vol. 19C, Part IV (1995), p. 397.

[12] Goniche, M. *et al.*, "Acceleration of electrons in the near field of lower hybrid frequency grills", in D. Gressilon, A. Sitenko and A. Zagorodny (Eds.), *Europhys. Conf. Abstr.*, vol. 20C, Part II (Kiev, Ukraine, 1996), pp. 783–786.

[13] Mailloux, J. *et al.*, "Strong toroidal asymmetries in power deposition on divertor and first wall components during LHCD on TdeV and Tore Supra", *J. Nucl. Mat.* **241–243** (1997), pp. 745–749.

[14] Evans, T. E., Neuhauser, J., Leuterer, F., Müller, E. R. and the ASDEX Team, "Characteristics of toroidal energy deposition asymmetries in ASDEX", *J. Nucl. Mat.* **176–177** (1990), pp. 220–207.

[15] Dobbing, J. A. *et al.*, "Power handling in the JET lower hybrid launcher", Tech. Rep. JET-R(97)06, JET Joint Undertaking (1997).

[16] Goniche, M. *et al.*, "Progress towards long pulse LH assisted operation with the ergodic divertor on Tore Supra", in J. Jacquinot, G. van Oost and R. R. Weynants (Eds.), *Europhys. Conf. Abstr.*, vol. 22A (Brussels, Belgium, 1998), pp. 129–132.

[17] Goniche, M. *et al.*, "Enhanced heat flux in the scrape-off layer due to electrons accelerated in the near field of lower hybrid grills", *Nucl. Fusion* **38** (1998), pp. 919–937.

[18] Brambilla, M., *Kinetic Theory of Plasma Waves*, no. 96 in International Series of Monographs on Physics (Clarendon Press, Oxford, 1998).

[19] Fuchs, V., Goniche, M., Demers, Y., Jacquet, P. and Mailloux, J., "Acceleration of electrons in the vicinity of a lower hybrid waveguide array", *Phys. Plasmas* **3** (1996), p. 4023.

[20] Fuchs, V. *et al.*, "Lower hybrid power dissipation by tokamak plasma edge electrons", in *Proceedings of 12th Topical Conference on Radiofrequency Power in Plasmas, Savannah* (APS, New York, 1997).

[21] Tskhakaya, D., Kuhn, S., Petrzílka, V. and Khanal, R., "Effects of fast electrons on the potential of a divertor plate", in C. Nieswand (Ed.), *Europhys. Conf. Abstr.*, vol. 23J (Maastricht, The Netherlands, 1999), pp. 537–540.

[22] Tskhakaya, D., Kuhn, S. and Petrzílka, V., "Simulation of particle acceleration in front of a lower-hybrid grill", in K. Szegö, T. N. Todd and S. Zoletnik (Eds.), *Europhys. Conf. Abstr.*, vol. 24B (Budapest, Hungary, 2000), pp. 352–355.

[23] Tskhakaya, D., Kuhn, S., Petrzílka, V. and Khanal, R., "Effects of energetic electrons on magnetized electrostatic plasma sheaths", *Phys. Plasmas* **9** (2002), pp. 2486–2496.

[24] Petrzílka, V. *et al.*, "Enhancement of electron acceleration in front of LH grills by random field effects", in J. Jacquinot, G. van Oost and R. R. Weynants (Eds.), *Europhys. Conf. Abstr.*, vol. 22A (Brussels, Belgium, 1998), pp. 149–152.

[25] Petrzílka, V., Fuchs, V., Mailloux, J., Goniche, M. and Söldner, F. X., "Electron acceleration in front of the JET and Tore Supra grills", in P. Pavlo (Ed.), *Europhys. Conf. Abstr.*, vol. 22C (Praha, 1998), pp. 1194–1197.

[26] Petrzílka, V. *et al.*, "Nonlinear electron acceleration in near antenna fields including effects of random fields", in J. W. Connor, E. Sindoni and J. Vaclavik (Eds.), *International School of Plasma Physics "Piero Caldirola", Theory of Fusion Plasmas* (Societa Italiana di Fisica, Bologna, Italy, 1999).

[27] Petrzílka, V. *et al.*, "Plasma biasing by fast particles generated in front of the CASTOR and Tore Supra tokamak LH grills", *Czech. J. Phys.* **49** (1999), pp. S127–140.

[28] Jacquet, P. *et al.*, "Effects of septa shape and plasma density on the electric field spectra of LH antennas", Tech. Rep. CCFM-RI-474e, Centre Canadien de Fusion Magnétique, Varennes, Québec, Canada (1997).

[29] Dawson, J. M., "Computer modeling of plasma: Past, present, and future", *Phys. Plasmas* **2** (1995), pp. 2189–2199.

[30] Birdsall, C. K. and Langdon, A. B., *Plasma Physics via Computer Simulation* (Institute of Physics Publishing Ltd, Bristol, England, 1991).

[31] Brambilla, M., "Slow-wave launching at the lower hybrid frequency using a phased waveguide array", *Nucl. Fusion* **16** (1976), pp. 47–54.

[32] Moreau, D., Gormezano, C., Melin, G. and Nguyen, T., "Density regimes for lower hybrid wave coupling in tokamak plasmas", in B. McNamara (Ed.), *Radiation in Plasmas*, vol. 1 (World Scientific, Singapore, 1984), pp. 331–349.

[33] Rantamäki, K. M., Pättikangas, T. J. H., Karttunen, S. J., Litaudon, X. and Moreau, D., "Simulations of fast particle generation by LH waves near the grill", in D. Gressilon, A. Sitenko and A. Zagorodny (Eds.), *Europhys. Conf. Abstr.*, vol. 20C, Part II (Kiev, Ukraine, 1996), pp. 875–878.

[34] Rantamäki, K. M., Lönnroth, J., Heikkinen, J. and Karttunen, S. J., "Particle-in-cell simulations of ion-Bernstein wave excitation", in J. W. Connor, O. Sauter and E. Sindoni (Eds.), *International School of Plasma Physics "Piero Caldirola", Theory of Fusion Plasmas* (Societa Italiana di Fisica, Bologna, Italy, 2000), pp. 457–462.

[35] Lönnroth, J. S., Heikkinen, J. A., Rantamäki, K. M. and Karttunen, S. J., "Particle-in-cell simulation of ion Bernstein wave excitation", *Phys. Plasmas* **9** (2002), pp. 2926–2939.

[36] Vahedi, V., Birdsall, C. K., Lieberman, M. A., DiPeso, G. and Rognlien, T. D., "Verification of frequency scaling laws for capacitive radio-frequency discharges using two-dimensional simulations", *Phys. Fluids* **B 5** (1993), p. 2719.

[37] Rantamäki, K. M., Pättikangas, T. J. H., Karttunen, S. J., Litaudon, X. and Moreau, D., "Simulation of a lower hybrid grill mouth by coupling SWAN and a particle-in-cell code", in J. Jacquinot, G. van Oost and R. R. Weynants (Eds.), *Europhys. Conf. Abstr.*, vol. 22A (Brussels, Belgium, 1998), pp. 173–176.

[38] Bibet, P. *et al.*, "Advanced launcher for lower hybrid current drive on Tore Supra", in B. Beaumont, P. Libeyre, B. de Gentile and G. Tonon (Eds.), *Fusion Technology 1998*, vol. 1 of *Proceedings of the 20th Symposium on Fusion Technology, Marseille, 1998* (Marseille, France, 1998), pp. 339–342.

[39] Rantamäki, K. M., Salmi, A. T. and Karttunen, S. J., "Particle-in-cell simulations for lower hybrid coupling near cut-off density", in *Europhys. Conf. Abstr.*, vol. 26B (2002), p. P4.106.

[40] Porkolab, M., "Survey of lower hybrid experiments", *IEEE Trans. Plasma Sci.* **PS-12** (1984), pp. 107–117.

[41] Gormezano, C., *Generation and Application of High Power Microwaves*, chap. RF Systems for Heating and Current Drive in Fusion Experiments, no. 48 in Scottish Universities Summer School in Physics (Scottish Universities Summer School in Physics and Institute of Physics Publishing, Bristol, Great Britain, 1997), pp. 275–304, also Report JET-P(96)57.

[42] Chen, F. F., *Introduction to Plasma Physics and Controlled Fusion*, vol. 1 (Plenum Press, New York, 1984), second edn.

[43] Stix, T. H., *Waves in Plasmas* (American Institute of Physics, New York, 1992).

[44] Stix, T. H., "Radiation and absorption via mode conversion in an inhomogeneous collision-free plasma", *Phys. Rev. Lett.* **15** (1965), pp. 878–882.

[45] Golant, V. E., "О Проникновении волн в плазму при частотах близких к нижней гибридной", *Журнал Технической Физики* **41** (1971) стр 2492–2503, Žhurnal Tekhničheskoj Fiziki, Journal of Technical Physics (in Russian).

[46] Kuehl, H. H., "Electromagnetic radiation from an electric dipole in an cold anisotropic plasma", *Phys. Fluids* **5** (1962), pp. 1095–1103.

[47] Fisher, R. K. and Gould, R. W., "Resonance cones in the field pattern of a short antenna in an anisotropic plasma", *Phys. Rev. Lett.* **22** (1969), pp. 1093–1095.

[48] Fisher, R. K. and Gould, R. W., "Resonance cones in the field pattern of a radio frequency probe in a warm anisotropic plasma", *Phys. Fluids* **14** (1971), pp. 857–867.

[49] Briggs, R. J. and Parker, R. R., "Transport of rf energy to the lower hybrid resonance in an inhomogeneous plasma", *Phys. Rev. Lett.* **29** (1972), pp. 852–855.

[50] Bellan, P. M. and Porkolab, M., "Experimental studies of lower hybrid wave propagation", *Phys. Fluids* **19** (1976), pp. 995–1006.

[51] Swanson, D. G., *Plasma Waves* (Academic Press, 1989).

[52] Landau, L., "On the vibrations of the electronic plasma", *Journal of Physics* **10** (1946), pp. 25–34.

[53] Malmberg, J. H. and Wharton, C. B., "Collisionless damping of electrostatic plasma waves", *Phys. Rev. Lett.* **13** (1964), pp. 184–186.

[54] Ichimaru, S., *Basic Principles of Plasma Physics, A Statistical Approach* (Benjamin/Cummings, Reading, Massachusetts, 1973).

[55] Porkolab, M., *Fusion*, vol. 1, Magnetic Confinement, Part B, chap. Radio Frequency Heating of Magnetically Confined Plasma (Academic Press, NY, 1981), pp. 151–191.

[56] Glagolev, V. M., "Propagation and absorption of ion hybrid waves in a weakly inhomogeneous plasma layer–I", *Phys. Plasmas* **14** (1972), pp. 301–314.

[57] Glagolev, V. M., "Propagation and absorption of ion hybrid waves in a weakly inhomogeneous plasma layer–II", *Phys. Plasmas* **14** (1972), pp. 315–326.

[58] England, A. C., Eldridge, O. C., Knowlton, S. F., Porkolab, M. and Wilson, J. R., "Power transmission and coupling for radiofrequency heating of plasmas", *Nucl. Fusion* **29** (1989), p. 1527.

[59] Bonoli, P., "Linear theory of lower hybrid heating", *IEEE Trans. Plasma Sci.* **PS-12** (1984), pp. 95–107.

[60] Chirikov, B. V., "A universal instability of many-dimensional oscillator systems", *Phys. Rep.* **52** (1979), p. 263.

[61] Berndtson, J. T., Heikkinen, J. A., Karttunen, S. J., Pättikangas, T. J. H. and Salomaa, R. R. E., "Analysis of velocity diffusion of electrons with Vlasov-Poisson simulations", *Plasma Phys. & Controlled Fusion* **36** (1994), pp. 57–71.

[62] Lallia, P., "A LHR heating slow wave launching structure suited for large toroidal experiments", in *Proceedings of the Second Topical Conference of RF Plasma Heating*, no. SR-5 in Texas Tech University Semicentennial 1973–1975 (Texas Tech University, Lubbock Texas, 1974).

[63] Moreau, D. and Nguyen, T. K., "Lower hybrid wave launching in large tokamaks", in M. Q. Tran and M. L. Sawley (Eds.), *Proceedings of the International Conference on Plasma Physics, Contributed Papers* (Lausanne, Switzerland, 1984), p. 216.

[64] Moreau, D. and Nguyen, T. K., "Couplage de l'onde lente au voisinage de la fréquence hybride basse dans les grands tokamaks", Tech. Rep. Report EUR-CEA-FC-1246, Centre d'études nucléaires de Grenoble (1984), (in French).

[65] Gormezano, C. *et al.*, "Lower hybrid plasma heating via a new launcher – the multijunction grill", *Nucl. Fusion* **25** (1985), pp. 419–423.

[66] Bibet, P. *et al.*, "Experimental and theoretical results concerning the development of the main rf components for next Tore Supra LHCD antennae", in K. Herschbach, W. Maurer and J. E. Vetter (Eds.), *Fusion Technology 1994*, vol. 1 (Elsevier, Amsterdam, 1995), pp. 577–580.

[67] Litaudon, X. *et al.*, "Lower hybrid wave coupling in Tore Supra through multijunction launchers", *Nucl. Fusion* **32** (1992), p. 1883.

[68] Bibet, P., Fuchs, V. and Litaudon, X., "Unequally spaced waveguide array for LHCD", in J. Jacquinot, G. van Oost and R. R. Weynants (Eds.), *Europhys. Conf. Abstr.*, vol. 22A (Brussels, Belgium, 1998), pp. 137–140.

[69] Bibet, P. *et al.*, "Coupling and power handling of the new Tore Supra LHCD launcher", *Fusion Eng. & Design* **56–57** (2001), pp. 679–684.

[70] Froissard, P. *et al.*, "Lower hybrid heating and current drive design for ITER and application for present tokamak", in B. Beaumont, P. Libeyre, B. de Gentile and G. Tonon (Eds.), *Fusion Technology 1998*, vol. 1 of *Proceedings of the 20th Symposium on Fusion Technology, Marseille, 1998* (Marseille, France, 1998), pp. 351–354.

[71] Bibet, P. and Mirizzi, F., "Report on ITER FEAT LHCD launcher", Tech. Rep. Contract FU05-CT-2001-00019 (EFDA/00-553), EFDA (2001).

[72] Mirizzi, F., Bibet, P., Marra, A., Petrolini, P. and Tuccillo, A. A., "The PAM launcher for FTU: Results of the preliminary tests", *Fusion Eng. & Design* To appear in Proceedings of 22nd Symposium on Fusion Technology, 9–11 September 2002, Helsinki, Finland.

[73] Litaudon, X., *Etude théorique et expérimentale du couplage de l'onde hybride dans Tore-Supra et JET au moyen d'antennes à multijonctions*, Ph.D. thesis, Université de Provence (Aix-Marseille I) (1990), (in French).

[74] Verboncoeur, J. P., Langdon, A. B. and Gladd, N. T., "An object-oriented electromagnetic PIC code", *Comp. Phys. Comm.* **87** (1995), pp. 199–211.

[75] Abe, H. and Itatani, R., "Propagation and plasma heating of the lower hybrid wave in the nonuniform density plasma", *Phys. Fluids* **22** (1979), p. 1533.

[76] Nakajima, N., Abe, H. and Itatani, R., "Energy and momentum deposition in plasmas due to the lower hybrid wave by a finite source", *Phys. Fluids* **25** (1982), p. 2234.

[77] Dumbrajs, O. *et al.*, "Local current profile modification in tokamak reactors in various radiofrequency ranges", in *Proceedings of the 16th International Conference on Fusion Energy, Montréal, Canada, October 7–11, 1996*, vol. 3 (IAEA, Vienna, 1997), pp. 373–380.

[78] Rantamäki, K., "*An Electrostatic Particle-in-Cell Model for a Lower Hybrid Grill*", Licentiate's thesis, Helsinki University of Technology, Report TKK-F-B175, Espoo (1998).

[79] Rantamäki, K. M. *et al.*, "Particle-in-cell simulations of power absorption in the near field of lower hybrid grills", in J. W. Connor, E. Sindoni and J. Vaclavik (Eds.), *International School of Plasma Physics "Piero Caldirola", Theory of Fusion Plasmas* (Societa Italiana di Fisica, Bologna, Italy, 1999), pp. 531–536.

[80] Rantamäki, K. M. *et al.*, "Interaction of LH-waves with scrape-off-layer electrons", *Czech. J. Phys.* **48** (1998), pp. S307–312.

[81] Heikkinen, J. A. *et al.*, "Parasitic particle acceleration and rf power absorption in edge plasmas", *Contrib. Plasma Phys.* **40** (2000), pp. 276–287.

[82] Bibet, P., Fuchs, V. and Mailloux, J., "Coupling properties and edge plasma interaction characteristics of the new Tore Supra lower hybrid antenna", in C. Nieswand (Ed.), *Europhys. Conf. Abstr.*, vol. 23J (Maastricht, The Netherlands, 1999), pp. 1009–1012.

[83] Gunn, J. *et al.*, "Particle recirculation in the ergodic divertor of Tore Supra", *Plasma Phys. & Controlled Fusion* **41** (1999), pp. B243–B257.

[84] Bibet, P. *et al.*, "Overview of the ITER-FEAT LH system", *Fusion Eng. & Design* To appear in Proceedings of 22nd Symposium on Fusion Technology, 9–11 September 2002, Helsinki, Finland.

[85] Airila, M. *et al.*, "Simulations of heat loads on plasma facing components", to appear in *Proceedings of the IAEA Conference on Controlled Fusion* (2002).

[86] Rantamäki, K. M. and Karttunen, S. J., "Particle-in-cell simulations for lower hybrid coupling and current drive", in C. Silva, C. Varandas and D. Campbell (Eds.), *Europhys. Conf. Abstr.*, vol. 25A (Madeira, Portugal, 2001), pp. 337–340.

[87] Rantamäki, K. M. *et al.*, "An electromagnetic particle-in-cell model for a lower hybrid launcher", in C. Nieswand (Ed.), *Europhys. Conf. Abstr.*, vol. 23J (Maastricht, The Netherlands, 1999), pp. 1653–1656.

[88] Rantamäki, K. M. *et al.*, "Particle-in-cell simulations of wave propagation in front of a lower hybrid grill", in K. Szegö, T. N. Todd and S. Zoletnik (Eds.), *Europhys. Conf. Abstr.*, vol. 24B (Budapest, Hungary, 2000), pp. 1196–1199.

[89] Litaudon, X. and Moreau, D., "Coupling of slow waves near the lower hybrid frequency in JET", *Nucl. Fusion* **30** (1990), p. 471.

[90] Rantamäki, K. M. and Karttunen, S. J., "Coupling study of JET LH grill", (2001), report on Notification Work for Task Force H, Unpublished.

[91] Ekedahl, A. *et al.*, "First results of coupling and edge plasma interaction experiments with the new advanced LHCD launcher in Tore Supra", in K. Szegö, T. N. Todd and S. Zoletnik (Eds.), *Europhys. Conf. Abstr.*, vol. 24B (Budapest, Hungary, 2000), pp. 800–803.

[92] Sato, K. and Miyawaki, F., "Sheath and heat flow of a two-electron-temperature plasma in the presence of electron emission", *J. Phys. Soc. Japan* **61** (1992), pp. 1453–1456, also Report NIFS–136 (1992).

[93] Harris, J. H. *et al.*, "Plasma-surface interactions with ICRF antennas and lower hybrid grills in Tore Supra", *J. Nucl. Mat.* **241–243** (1997), pp. 511–516.

[94] Asano, K., Ohno, N., Ye, M. E., Fukuta, S. and Takamura, S., "2-D PIC simulation of space-charge limited emission current from plasma-facing components", *Contrib. Plasma Phys.* **40** (2000), pp. 478–483.

[95] Dux, R., Ingesson, C., Giroud, C. and Zastrow, K., "Impurity behaviour in ITB discharges with reversed shear on JET", in C. Silva, C. Varandas and D. Campbell (Eds.), *Europhys. Conf. Abstr.*, vol. 25A (Madeira, Portugal, 2001), pp. 505–508.

[96] ITER home page, "http://www.iter.org/", web-page (2003).

Appendix A

Plasma Parameters

Table A.1: Typical tokamak parameters [2, 4, 96].

		Tore Supra	JET	ITER
Major radius	R [m]	2.4	2.96	6.2
Minor radius	a [m]	0.75	1.25	2.0
Plasma volume	V [m^3]	25	85	837
Toroidal magnetic field at centre	B_T [T]	4	3.5	5.3
Plasma current	I_p [MA]	2	7	15
Additional heating power	P_add [MW]	25	47	73

Table A.2: Plasma parameter ranges used in the simulations of this work.

		Tore Supra	JET	ITER
Plasma density	n_e [10^{18} m^{-3}]	0.6 - 2.0	0.3 - 3.0	6.2
Plasma temperature	T_e [eV]	12.5 - 100	25	25
Magnetic field	B [T]	2.78	2.2	4
Grill frequency	f [GHz]	3.7	3.7	5
Angular frequency	ω [10^{10} 1/s]	2.32	2.32	3.14
Plasma frequency	ω_pe [10^{10} 1/s]	4.37 - 7.98	3.09 - 9.77	1.40
Cyclotron frequency	Ω_ce [10^{11} 1/s]	4.89	3.87	7.03
LH resonance frequency	ω_LH [10^9 1/s]	0.72 - 1.30	0.51 - 1.56	2.27
	$\omega/\omega_\mathrm{LH}$	17.9 - 32.4	14.9 - 45.7	13.8
Thermal velocity	v_the [10^6 m/s]	2.10 - 5.93	2.97	2.97
Debye length	λ_De [10^{-5} m]	3.72 - 10.5	3.03 - 9.60	2.11
Larmor radius	r_Le [10^{-6} m]	4.29 - 12.1	7.66	4.22
Collision frequency	$\nu_\perp^{\mathrm{e/i}}$ [10^6 1/s]	0.11 - 2.2	0.26 - 2.4	4.8

Published by

Series title, number and report code of publication

VTT Publications 493
VTT–PUBS–493

Author(s)
Rantamäki, Karin

Title

Particle-in-Cell Simulations of the Near-Field of a Lower Hybrid Grill

Abstract

Lower hybrid (LH) waves in the frequency range 1 to 10 GHz are used to heat and to drive current in a tokamak. A crucial issue for the future devices is the coupling of the wave power from the launching structure, the grill, to the plasma. A related problem is the formation of hot spots on the grill limiters and other components that are magnetically connected to the grill region. A probable explanation for these asymmetric heat loads is the parasitic absorption of the LH power. In parasitic absorption, the short-wavelength modes are absorbed by electrons within a very short distance in front of the grill. The cold edge electrons ($T_e \sim 25$ eV) may reach energies up to 2 keV through stochastic acceleration in the electric field in front of the lower hybrid grill.

The particle-in-cell (PIC) technique is one of the most popular methods of kinetic simulations of plasmas. In PIC codes, a spatial grid is used to describe the field quantities, while the particles move in the continuous space. The field and particle motion are solved self-consistently. The advantage of the PIC codes is that they take into account the kinetic effects and the non-linearities of the problem. They also give the deposition profiles unlike pure test particle simulations.

In this thesis, the use of PIC codes has been extended to a whole new branch of applications, the near-field of the LH grill. During the work, the grill model used in the electrostatic PIC code has been developed. The parasitic absorption and the generation of fast electrons in front of the waveguide mouth have been explored. The absorption and the heat load on the grill limiter increases with the edge density, the edge temperature and the launched power density. A weak indication of a power threshold was observed. The simulation results can explain experimental observations in Tore Supra. According to the simulations, the heat loads are not a problem in the next generation launchers used in ITER.

Keywords
plasma heating, microwaves, lower hybrid grill, lower hybrid waves, particle-in-cell simulation, parasitic absorption, wave coupling, thermonuclear devices, Tore Supra, tokmak, JET, current drive, nuclear fusion

Activity unit
VTT Processes, Otakaari 3 A, P.O.Box 1608, FIN–02044 VTT, Finland

ISBN			Project number
951–38–6040–X (soft back ed.) 951–38–6041–8 (URL:http://www.inf.vtt.fi/pdf/)			
Date	Language	Pages	Price
April 2003	English	74 p. + app. 61 p.	C
Name of project		Commissioned by	
Series title and ISSN VTT Publications 1235–0621 (soft back ed.) 1455–0849 (URL: http://www.inf.vtt.fi/pdf/)		Sold by VTT Information Service P.O.Box 2000, FIN–02044 VTT, Finland Phone internat. +358 9 456 4404 Fax +358 9 456 4374	

The world energy demand is predicted to double or triple in the next 50 years. All the possible know-how as well as a variety of benign energy production methods are needed to solve the energy problem. No single power production method by itself can meet the energy need. Renewable energy sources, nuclear fission and fusion could together provide a sustainable solution for the power production, as the fossil fuels, which produce CO_2, are exhausted. The main advantage of fusion is that it has unlimited fuel sources – a few litres of seawater corresponds to a barrel of oil. In fusion, two light nuclei fuse together forming a heavier nucleus and releasing energy. This is the energy source of the sun and other stars. The most promising device for a fusion reactor is the tokamak – a doughnut-shaped device where the 100-million-degree-hot fuel is confined magnetically. The high temperature can be achieved by injecting energetic particle beams or radio-frequency (RF) waves, which are used in three different frequency ranges. In this thesis, the RF waves at a few GHz are studied. The focus is on the interaction of the waves with particles in front of the launcher. The particles are accelerated by the wave and travel to wall structures where they cause high heat loads. These heat loads may damage the components and are especially inconvenient in long-pulse discharges because they limit the allowed power level. The work is related to the RF-experiments carried out at JET (Joint European Torus) in UK and Tore Supra in France. Predictions for ITER have also been made.

Tätä julkaisua myy

VTT TIETOPALVELU
PL 2000
02044 VTT
Puh. (09) 456 4404
Faksi (09) 456 4374

Denna publikation säljs av

VTT INFORMATIONSTJÄNST
PB 2000
02044 VTT
Tel. (09) 456 4404
Fax (09) 456 4374

This publication is available from

VTT INFORMATION SERVICE
P.O.Box 2000
FIN–02044 VTT, Finland
Phone internat. +358 9 456 4404
Fax +358 9 456 4374

ISBN 951–38–6040–X (nid.)
ISSN 1235–0621 (nid.)

ISBN 951–38–6041–8 (URL: http://www.inf.vtt.fi/pdf/)
ISSN 1455–0849 (URL: http://www.inf.vtt.fi/pdf/)

VTT PUBLICATIONS 493 Particle-in-Cell Simulations of the Near-Field of a Lower Hybrid Grill Karin Rantamäki